



A high resolution coupled ocean-atmosphere simulation of the regional climate over Central America

Vasubandhu Misra^{1,2,3} · C. B. Jayasankar^{2,3}

Received: 4 June 2021 / Accepted: 26 November 2021

© The Author(s), under exclusive licence to Springer-Verlag GmbH Germany, part of Springer Nature 2021

Abstract

This study analyzes a relatively high resolution (15 km grid spacing), regional coupled ocean–atmosphere simulation configured over Central America. The simulation is conducted with the Regional Spectral Model-Regional Ocean Model System (RSM-ROMS) forced with global atmospheric and oceanic reanalysis for a period of 25 years (1986–2010). The spatial resolution of the RSM-ROMS simulation is unprecedented for the region. The highlights of the RCM simulation include the verifiable seasonal cycle of mesoscale features like the Low-Level Jets (LLJs), the Mid-Summer Drought (MSD), and the seasonal Tropical Cyclone (TC) activity both in the Pacific and in the Atlantic Oceans. However, some of the biases of the RSM-ROMS simulation of the frequency and amplitude of the MSD, the track density of the TCs in the two ocean basins, and the seasonal bias of the LLJs are noted. The seasonal cycle of the robust surface ocean currents in the eastern Pacific and the Costa Rica Dome is also well captured in the RSM-ROMS simulation. The RSM-ROMS simulation also resolves the seasonal cycle of the cyclonic Panama-Colombia Gyre and the anti-cyclonic Gulf of Papagayo-Tehuantepec Gyre. In many instances we find the RSM-ROMS improves upon the global reanalysis forcing the simulation, indicating the potential value of dynamic downscaling. Furthermore, the co-evolving components of the atmosphere and ocean in the RCM is an added benefit to the atmosphere only and ocean only global reanalysis forcing the simulation. However, the RCM displays significant biases that manifest in precipitation, precipitable water, SST, and winds which in the cases of prognostic variables of RSM-ROMS are perpetrated by the biases in the lateral boundary forcing (e.g., precipitable water) and in other instances forced by biases within the RSM-ROMS (e.g., precipitation, SST).

1 Introduction

The Central American Isthmus (CAI) is by far one of the most challenging areas for climate modeling. It is a narrow strip of land, which is approximately 50 km wide at its narrowest, beset with narrow range of mountains and surrounded by oceans along its eastern and western coast (Fig. 1). The isthmus is periodically affected by natural threats engendered by a prolonged season of Tropical Cyclone (TC) activity from both the Caribbean Sea and the eastern Pacific Ocean. For example, Hurricane Mitch

of 1998, devastated Honduras with over 11,000 fatalities (Morris et al. 2002). Similarly, Afonso (2011) and Spencer and Urquhart (2018) indicate that there is significant human migration from Central American countries to the United States as an aftermath to landfalling TCs in the region. Besides TCs, the region is well known for many Low Level Jets (LLJs) that are caused by gaps in the mountain ranges of Central America. These LLJ's can sometimes produce low level vorticity, which in conjunction with either the Inter-Tropical Convergence Zone (ITCZ) and or the prevalent monsoon trough can lead to tropical cyclogenesis in the tropical eastern Pacific Ocean (Heather and Bourassa 2014).

Maldonado et al. (2018) suggest that apart from the intense, relatively infrequent events of landfalling TCs, the higher frequency meteorological events of lower intensity can also cause severe impacts in the region. For example, the synoptic disturbances emanating from the ITCZ affect the Pacific side of Central America (Hidalgo et al. 2015; Quirós-Badilla and Hidalgo-Leon 2016), the rainfall production from cold surges sometimes produce extreme precipitation

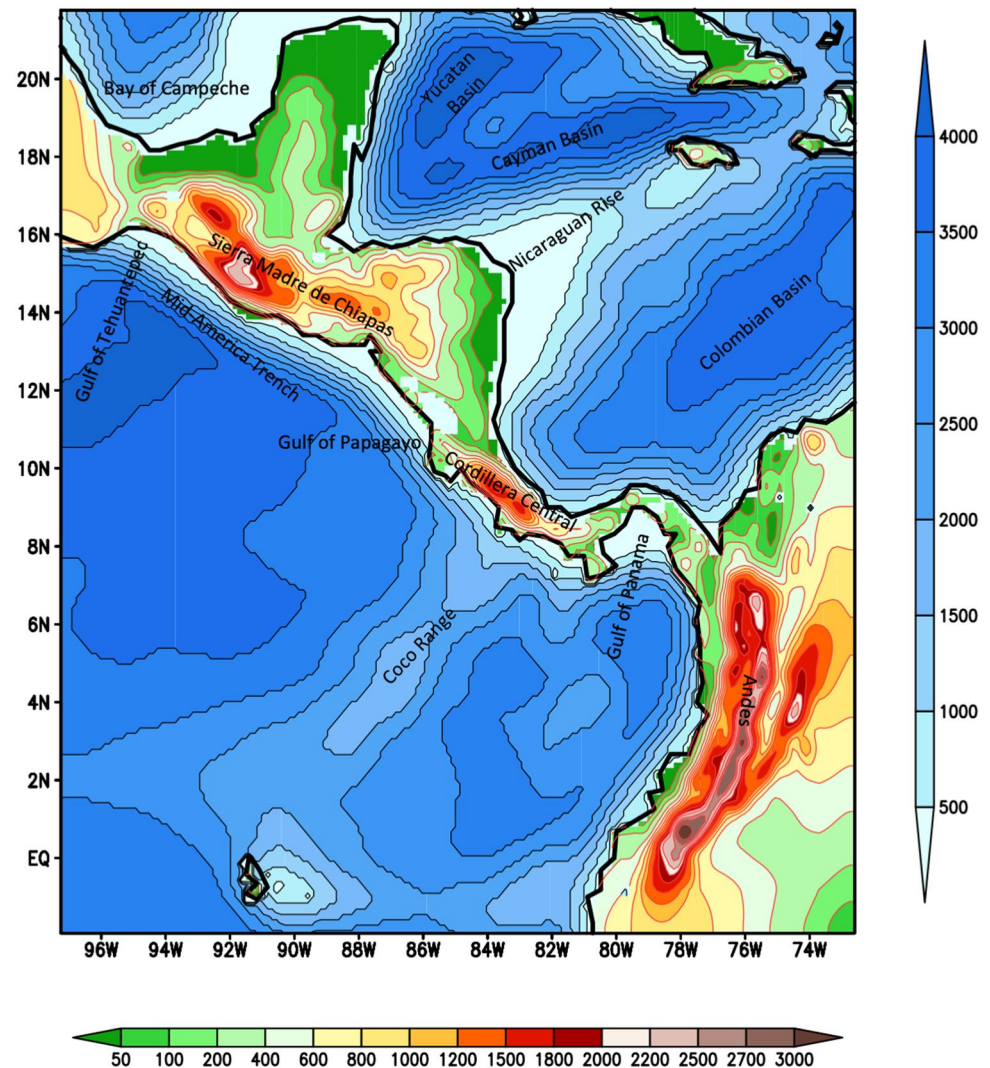
✉ Vasubandhu Misra
vmisra@fsu.edu

¹ Department of Earth, Ocean and Atmospheric Science, Florida State University, Tallahassee, FL, USA

² Center for Ocean-Atmospheric Prediction Studies, Florida State University, Tallahassee, FL, USA

³ Florida Climate Institute, Florida State University, Tallahassee, FL, USA

Fig. 1 The ocean bathymetry (color bar on the right) and land topography (color bar at the bottom) of the regional domain of RSM-ROMS used in the study. Some bathymetric features and geographical locations referenced in the text are noted in the figure. The units are in meters



in the dry winter and early summer climate of the north and Caribbean coast of Costa Rica and Honduras (Schultz et al. 1998; Retana 2012), the westward propagation of tropical disturbances in the summer (Amador et al. 2016), and the mid-summer drought (Magana et al. 1999).

The eastern Pacific Ocean in the west and the Gulf of Mexico and the Caribbean Sea to the east of the CAI is part of the Intra-Americas Seas (IAS). The IAS is host to the second largest body of warm water (≥ 28.5 °C) on Earth and hosts the second largest diabatic heating center of the tropics during the boreal summer (Wang and Enfield 2001). Overlying the IAS, on the Atlantic side is the North Atlantic Subtropical High (NASH), which display a distinct seasonal cycle (Davis et al. 1996). The equatorward flank of the NASH comprises of the easterly trades of the Atlantic, which has a strong bearing on the moisture flux into the CAI as these trade winds accelerate in the Caribbean Sea to form the Caribbean LLJ (CLLJ; Amador and Magana 1999; Poveda and Mesa 1999; Wang 2007; Gimeno et al. 2012; Misra

et al. 2014). Similarly, in the Pacific side, resides the North Pacific subtropical high, which also carries the north easterly trades but away from the CAI. Xie et al. (2008) suggest that variations in the tropical Atlantic Ocean can affect tropical Pacific by way of the atmospheric bridge across Central America. For example, the cold phase of the Atlantic Multidecadal Oscillation is observed to reduce the amplitude of the seasonal cycle in SST and surface winds over the equatorial Pacific (Timmermann et al. 2007). Similarly, Xie et al. (2008) indicate that cooling of the North Atlantic SST suppresses atmospheric convection over Central America and tropical eastern Pacific Ocean. Likewise, the mid-summer drought over Central America observed in July–August amidst their wet season before it recovers in September is a result of the variations of NASH initiated by anomalies in the north tropical Atlantic Ocean (Mapes et al. 2005; Xie et al. 2008). More recently, Corrales-Suastegui (2020) suggest that the negative differential warming between the tropical Atlantic and eastern Pacific Ocean (i.e., warmer

eastern Pacific Ocean and colder tropical Atlantic) can lead to further severity of the mid-summer drought in a future climate under the highest emission scenario (i.e., Reference Concentration Pathway[RCP]8.5).

The Costa-Rica Dome located off the west coast of Central America is the shoaling of a generally strong and shallow thermocline in the region. It is a ‘permanent’ feature that is centered around 9°N and 90°W, about 300 km off the Gulf of Papagayo between Costa Rica and Nicaragua (Wyrski 1964). As a result of this ridging of the thermocline, the Costa Rica Dome is a region of high primary productivity as nutrients are brought up to the surface by wind mixing and upwelling (King 1986). However, there is significant variability of this dome both with its location and magnitude because of the wind variations associated with the Inter-Tropical Convergence Zone (ITCZ) and the surface ocean currents (Fiedler 2002). Seasonally, the Costa Rica Dome is shallower in the boreal summer-fall seasons when the ITCZ is over the dome and local winds are weak. In the boreal winter season, the Costa Rica Dome is deeper when the ITCZ is south of the dome and the northeasterly trades are stronger. However, it may be noted that like any other tropical thermal dome, the Costa Rica Dome is associated with the cyclonic turning of zonal surface currents following geostrophic balance. In the case of the Costa Rica Dome, these zonal surface currents in the east Pacific are the North Equatorial Counter Current to the south and the North Equatorial Current to the north of the dome.

Given this rich amalgam of atmospheric and oceanic features of Central America, we are motivated to conduct a regional coupled ocean–atmosphere integration at an unprecedented spatial resolution of 15 km grid spacing to assess the fidelity of the model in simulating distinct atmospheric and oceanic features. In contrast, recent regional downscaling experiments over Central America are coarser in spatial resolution and are downscaling just the atmospheric component (e.g., Cavazos et al. 2020; Corrales-Suastegui et al. 2020; Torres-Alavez et al. 2021). There are, however, fewer studies that have been conducted with a regional coupled ocean–atmosphere model for Central America at a relatively high resolution (≤ 30 km). A coupled regional climate model integration over this region was conducted in Xie et al. (2008), which was over an 8 year period at 0.5° grid spacing. In this study, the regional climate model integration is conducted by forcing at the lateral boundaries with global atmospheric and oceanic reanalysis for a period of 25 years from 1986–2010. More recently, Cabos et al. (2019) used a regional atmosphere model coupled to a global ocean model to examine the climate simulation over Central America. Some of their main conclusions with 25 and 50 km atmospheric model grid resolution coupled to 10 km ocean grid include significant improvement of the ITCZ and the CLLJ from the inclusion of air–sea coupling

in comparison to the driving model fields that included much coarser global atmospheric reanalysis and coupled global model simulation. In the following section we describe the regional climate model. In Sect. 3, we discuss the details of the model integration along with the validation datasets used in the study. We present the results in Sect. 4 followed by concluding remarks in Sect. 5

2 Model description

The model used for this study is the Regional Spectral Model-Regional Ocean Modeling System (RSM-ROMS). RSM-ROMS is a regional, coupled ocean–atmosphere model that has been extensively used for regional climate modeling studies (Li et al. 2014; Li and Misra 2014; Ham et al. 2016; Misra et al. 2018). The atmospheric component of RSM-ROMS is RSM that was first introduced in Juang and Kanamitsu (1994). RSM uses the spectral method to compute advective derivatives using sine and cosine functions in two dimensions with wall boundary conditions (Tatsumi 1986). RSM uses the semi-implicit time integration scheme. The RSM has 28 terrain following sigma levels, with irregular spacing in the vertical that is identical to the National Centers for Environmental Prediction–Department of Energy (NCEP-DOE) Reanalysis (R2; Kanamitsu et al. 2002), and the top of the atmosphere in RSM is at approximately at 2 hPa. The physics package used in RSM for this study is outlined in Table 1. Selman and Misra (2015) conducted a detailed comparison of the convection schemes and lateral boundary forcing using the RSM over the Southeastern United States to conclude that Kain-Fritsch (KF; Kain and Fritsch 1993) and the Relaxed Arakawa Schubert scheme (RAS; Moorthi and Suarez 1992) performed equally well with R2 reanalysis lateral boundary conditions. However, the KF scheme makes RSM to integrate much slower than RAS convection scheme, which made our choice of using RAS as the choice of convection scheme for this study.

Table 1 Outline of the physical parameterization schemes used in RSM

Atmospheric model (regional spectral model)	Reference
Gravity wave drag	Alpert et al. (1988)
Boundary layer	Hong and Pan (1996)
Clouds	Zhao and Carr (1997)
Deep convection	Moorthi and Suarez 1992
Land surface model	Ek et al. (2003)
Longwave radiation	Chou et al. (1999)
Shortwave radiation	Chou and Lee (1996)
Shallow convection	Tiedtke (1983)

Similarly, Misra et al. (2017) found that Zhao and Carr prognostic cloud scheme (Zhao and Carr 1997) provided a simulation of the Indian Summer Monsoon (ISM) that showed higher fidelity than previous simulations of the ISM from RSM-ROMS that used the diagnostic Slingo cloud scheme (Glazer and Misra 2018). Therefore, we adopted Zhao and Carr prognostic cloud scheme for this study. The other choices of the RSM physics listed in Table 1 are dictated by the availability of only the listed schemes in the model. The scale selective bias correction (Kanamaru and Kanamitsu 2007, Kanamitsu et al. 2010) is used to prevent synoptic scale drift during the integration of RSM. Additionally, we have also increased the width of the sponge zone from the 8 grid points around the lateral boundaries used in the previous studies (e.g., Misra et al. 2018) to 16 grid points in this study. This was done after extensive model integrations, which showed that RSM displayed the most skill in reproducing the observed climate at a sponge width of 16 grid points (not shown).

ROMS is the oceanic component of RSM-ROMS. ROMS is a free surface, terrain following primitive equation ocean model (Haidvogel et al. 2000; Shchepetkin and McWilliams 2005). The equations are solved using the split explicit time-stepping scheme. The primitive equations are discretized in the vertical by using stretched, terrain following coordinates with 30 levels. The ROMS contain several subgrid scale parameterizations, which include local closure schemes based on the level 2.5 turbulent kinetic energy equations (Mellor and Yamada 1982) and generic length-scale parameterization following Umlauf and Burchard (2003). For this study, we used the second order biharmonic horizontal diffusion in ROMS (Ezer et al. 2002). The nonlocal closure scheme is based on the K profile, boundary layer formulation developed by Large et al. (1994). The K profile scheme has been expanded to include both surface and bottom oceanic boundary layers.

RSM and ROMS are coupled with a coupling interval of 1-h. The resolution of RSM and ROMS for this study is set at 15 km and is identical for both model components. Therefore, no flux coupler is used, and the atmospheric fluxes and SST are exchanged directly without any interpolation between the two model components at every hour of the model integration. Furthermore, there is no flux correction used in the model integration of RSM-ROMS.

3 Design of experiment

The model domain used for this study is shown in Fig. 1. As mentioned earlier, the horizontal grid spacing of RSM-ROMS is 15 km with the center of the grid at 85°W and 10°N with 181 and 178 grid points in the zonal and meridional directions, respectively. The model domain extends

from 1.93°S to 21.77°N and 72.46°W to 97.26°W, which includes the sponge zone. The orography used in RSM is interpolated to the domain grid from the Global 30 Arc-Second Elevation (Danielson and Gesch 2011), which equates to a resolution of approximately 1 km (Webster et al. 2003). Similarly, the ocean bathymetry used in ROMS is from 2-min gridded global relief data from NOAA National Geophysical Data Center (2006). The orography over land and the bathymetry in the ocean for the RSM-ROMS domain and resolution used in the study with notable features labeled are shown in Fig. 1. The fine scale resolution of RSM-ROMS at 15 km grid spacing is apparent in Fig. 1 with several of the steep bathymetric and orographic features resolved in the model.

The initial and lateral boundary conditions of the atmosphere are supplied to RSM from R2. The lateral boundary conditions of RSM are provided at intervals of 6 h. The ocean initial and lateral boundary conditions are provided from Simple Ocean Data Assimilation version 2. 2. 4 (SODA; Carton and Giese 2008). RSM-ROMS is integrated from 1st January 1986 through 31st December 2010.

The model verification and analysis are conducted in a domain that emphasizes the CAI. Therefore, the regional domain over which the model results are analyzed is limited to 0°–21°N and 74°W–96°W. To verify the RSM-ROMS integration we make use of the daily rainfall data from the Integrated Multi-satellite Retrievals for Global Precipitation Mission version 6 (IMERG; Huffman et al. 2019). This rainfall data is available globally at 0.1° grid spacing from 01 June 2000 to the present. Although, this data set does not overlap with the integration period of RSM-ROMS (1986–2010), it still provides us a robust 20 year climatology covering both land and the oceans at a resolution that is comparable to RSM-ROMS. In addition, we use the Climate Prediction Center (CPC) daily rainfall data following Xie et al. 2007 and Chen et al. 2008. This rainfall data is available only over land and from 1979 to the present (which overlaps with the integration period of RSM-ROMS) and is at 0.5° grid spacing. The CPC rainfall data is rain gauge based analysis. We also make use of the total precipitable water from the NASA Water Vapor Project (NVAP; https://eosweb.larc.nasa.gov/sites/default/files/project/nvap/readme/ASDC_NVAP_Overview_2016.pdf; https://doi.org/10.5067/NVAP-M/NVAP_CLIMATE_Total-Precipitable-Water_L3.001) to verify the precipitable water from the RSM-ROMS integration. The NVAP dataset is available globally from 1988 to 2009 at 1° grid spacing. For the verification of the model simulated SST, the NOAA Optimally Interpolated SST version 2 (OISSTv2; Reynolds et al. 2007) dataset is used. This dataset is available from 1981 to the present at 0.25° grid spacing at daily interval. The Climate Forecast System Reanalysis (CFSR; Saha et al. 2010) data is used for the validation of the upper air simulations. CFSR is available

globally at 0.5° grid spacing on 17 mandatory pressure levels. We also verify the upper ocean heat content measured as the depth of the 20°C isotherm and the wind stress from the model simulation against the SODA reanalysis data (Carton and Giese 2008). The best track data of TCs both in the Caribbean Sea and in the eastern Pacific Ocean from the model simulation are verified against HURDAT2 (Landsea and Franklin 2013). The tracks of the TCs are plotted from both these datasets at six-hour interval following the tracking algorithm of Ullrich and Zarzycki (2017).

4 Results

4.1 The seasonal cycle of rainfall

The seasonal cycle of the observed rainfall shows distinct dry (Fig. 2a, b) and wet (Fig. 2c, d) halves of the year over the CAI, coinciding with the boreal winter/spring and summer/fall seasons, respectively. The Inter-Tropical Convergence Zone (ITCZ) over northeastern Pacific Ocean appears very strong in June–July–August (JJA; Fig. 2c), which also coincides with the seasonal peak of rainfall over the CAI. The corresponding seasonal cycle of the rainfall from RSM-ROMS is shown in Fig. 2e–h and its systematic errors in Fig. 2i–l and Fig. 3a–c. From these figures we observe that although RSM-ROMS shows the seasonal peak of the ITCZ in the JJA season (Fig. 2g), it underestimates the seasonal ITCZ rainfall in the spring (Figs. 2j and 3a), summer (Figs. 2k and 3a), and fall (Figs. 2l and 3a) seasons while overestimating in the winter season (Figs. 2i and 3a). However, the seasonal variability in the latitudinal width of the near rain free zone over the eastern Pacific cold tongue region (Fig. 2a–d) is nicely replicated in RSM-ROMS (Fig. 2e–h). Over the Caribbean Sea, RSM-ROMS systematically overestimates (Figs. 2i–k and 3c) except in the September–October–November (SON) season, when the model shows underestimation along the Caribbean coast of Central America (Figs. 2k and 3c). An important difference in the systematic errors of rainfall displayed by RSM-ROMS between that over the tropical Pacific Ocean and the Caribbean Sea is that in the latter, the errors are less widespread spatially and are more homogeneous. However, over the tropical Pacific Ocean, the negative bias in the ITCZ region is nearly matched by the positive bias of rainfall in RSM-ROMS over the Gulf of Papagayo.

Over land, RSM-ROMS uniformly overestimates rainfall across CAI throughout the year (Figs. 2i–l and 3b). It is however important to recognize that the observed estimates of rainfall from IMERG and CPC rainfall analysis also differ significantly (Fig. 3b). In a comprehensive intercomparison of observed rainfall analyses, Sun et al. (2018) concluded that largest uncertainties occur in mountainous regions and

in regions of sparse data coverage. On the other hand, several studies suggest that satellite based rainfall over mountainous terrain can be less accurate because of high spatial variability of precipitation combined with low spatial resolution retrievals of from multi-satellite sensors, systematic biases of sensor technology, applied algorithm, precipitation type, and temporal sampling (Hirpa et al. 2010; Condom et al. 2011; Behrangi et al. 2014; Shige et al. 2017). Therefore, it is important to recognize the uncertainty of the observed estimates of rainfall over CAI. Regardless of this observed uncertainty, RSM-ROMS has clearly a wet bias (Fig. 3b) that is exacerbated most in the summer (Figs. 2k and 3b) and fall (Figs. 2l and 3b) seasons. Nonetheless the signature mid-summer drought of the CAI with slight dip in rainfall in July and August preceded by peak in rainfall in June and followed by another peak in September is nicely simulated in RSM-ROMS (Fig. 3b). We will discuss the rainfall from R2 shown in Fig. 3a–c later, in Sub-section h.

4.2 The seasonal cycle of precipitable water

The observed seasonal cycle of the precipitable water (Fig. 4a–d) closely follows that of rainfall (Fig. 2a–d), which is well depicted in the RSM-ROMS simulation (Fig. 4e–h). The north–south gradient of precipitable water across the domain throughout the year is quite similar in both observations (Fig. 4a–d) and RSM-ROMS (Fig. 4e–h). Furthermore, the maxima of the precipitable water in the ITCZ region of the tropical eastern Pacific throughout the year is also captured in the RSM-ROMS simulation, albeit underestimated. However, over the tropical Pacific the bias in RSM-ROMS is negative throughout the year (Figs. 4i–l and 3d). A widespread dry bias of the atmospheric column develops across the domain in JJA (Figs. 4k and 3d–f) and SON (Fig. 4l and Figs. 3d–f) seasons. The signature peaks of the mid-summer drought over CAI in precipitable water is also picked by the RSM-ROMS simulation (Fig. 3e), which coincides with the observed peaks of precipitation of the mid-summer drought feature (Fig. 3b). We will discuss the precipitable water from R2 shown in Fig. 3d–f later, in Sub-section h.

4.3 The seasonal cycle of SST

The observed SST in Fig. 5a–d show a robust seasonal cycle in both the tropical eastern Pacific Ocean and in the tropical Atlantic Ocean. For example, the coastal oceans of CAI both along the Pacific and the Atlantic sides exhibit coldest SST in DJF (Fig. 5a) and warmest SST in JJA (Fig. 5c). Furthermore, the cold tongue in the eastern equatorial Pacific Ocean widens and becomes colder in the JJA (Fig. 5c) and in the SON (Fig. 5d) seasons relative to DJF (Fig. 5a) and MAM (Fig. 5b) seasons. This seasonal cycle of the SST is reasonably captured in the RSM-ROMS simulation (Fig. 5e–h),

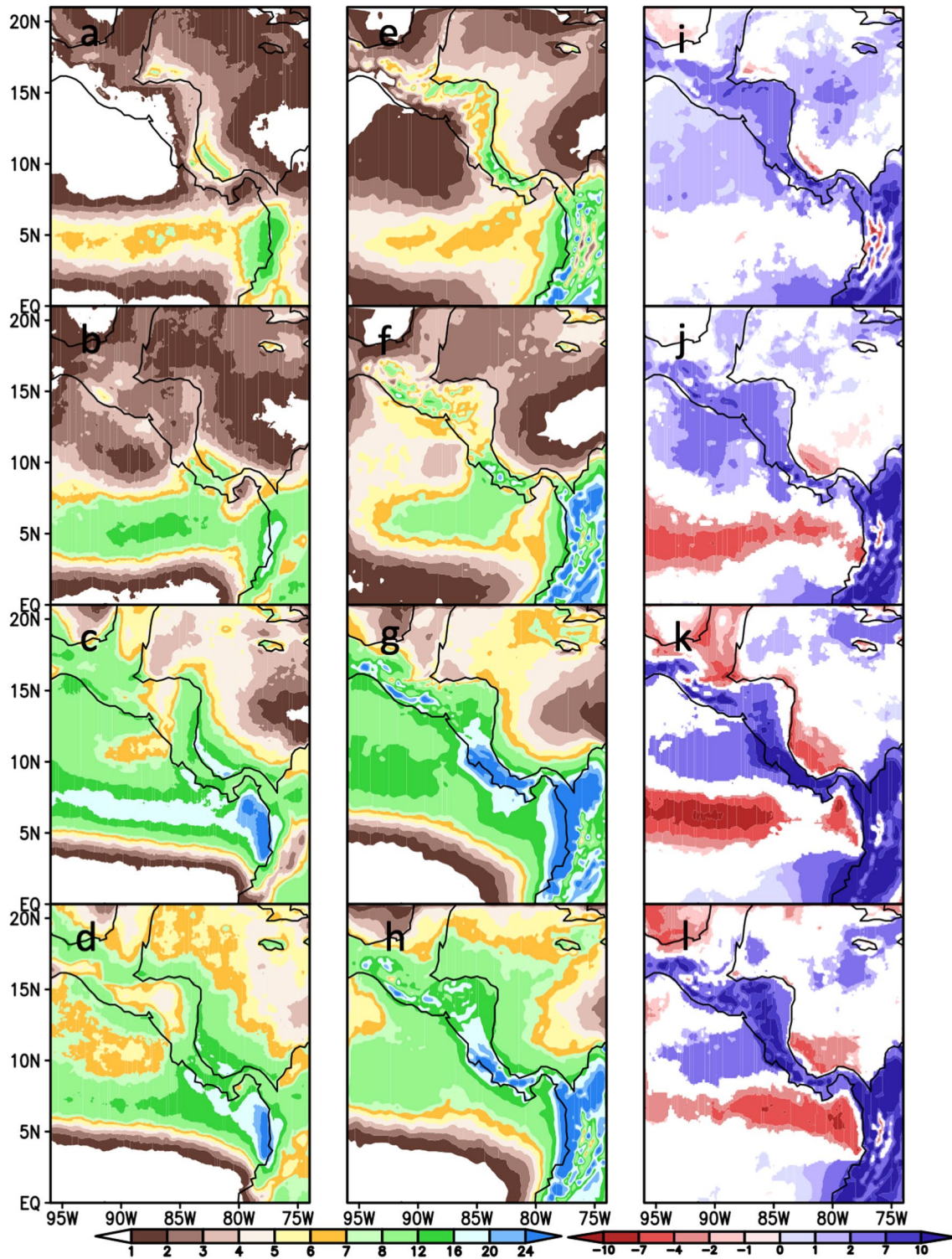


Fig. 2 The seasonal climatological rainfall (mm day^{-1} ; shaded) from **a, b, c, d** observations (IMERG) and **e, f, g, h** RSM-ROMS for **a, e** December–January–February, **b, f** March–April–May, **c, g** June–

July–August, and **d, h** September–October–November seasons. The corresponding seasonal systematic errors (shaded only if they exceed 95% confidence interval) of RSM-ROMS is shown in **(i, j, k, and l)**

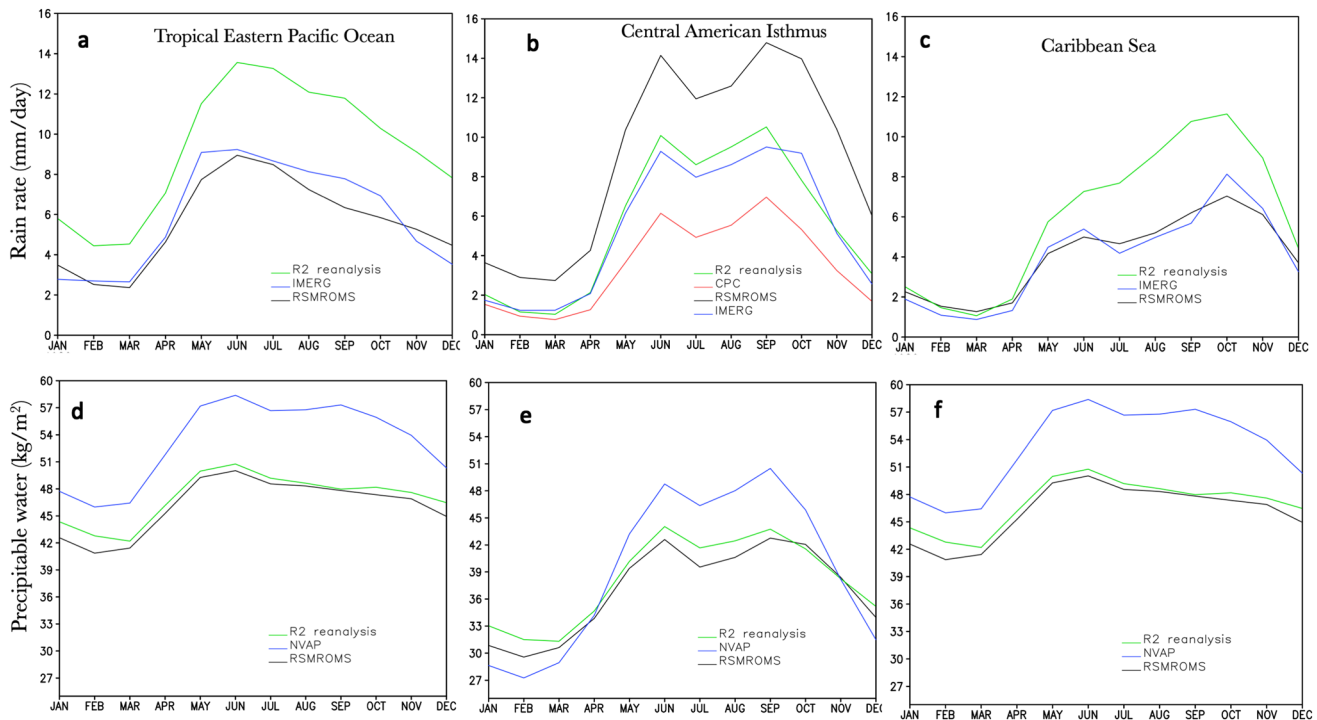


Fig. 3 The monthly mean climatology of **a, b, c** precipitation and **d, e, f** precipitable water over **a, d** tropical eastern Pacific Ocean (95°W to 78°W and 0° to 14°N, west of the Central American Isthmus), **b, e** Central American Isthmus (only land points within 95°W to 78°W

and 6°N to 21°N), and **c, f** Caribbean Sea (only ocean points west of the Central American Isthmus within 95°W to 75°W and 9°N to 21°N)

although the cold bias is apparent (Fig. 5i–l). The systematic errors of SST (Fig. 5i–l) reveal that in addition to the cold bias over the cold tongue in the equatorial Pacific, RSM-ROMS displays a persistent cold bias along the Pacific coast of CAI and over Colombian Basin in the Caribbean Sea. The systematic errors over the Cayman and the Yucatan Basins shift from a cold bias in DJF (Fig. 5i) to a warm bias in JJA (Fig. 5k) before it diminishes in SON (Fig. 5l).

An iconic feature of the region is the Costa Rica Dome, which shoals from west to east between the westward flowing North Equatorial Current (NEC) to the north and the eastward flowing North Equatorial Counter Current (NECC) to the south with the Costa Rican Counter Current (CRCC) along its eastern boundary (Fig. 6). This is observed in the monthly climatology of the depth of the 20 °C isotherm (a proxy for the depth of the thermocline; Fiedler 2002) from the SODA reanalysis, with the dome appearing in the Gulf of Papagayo in January–March, moving offshore during April–July, intensifying in July–November, before it begins to diminish in December–January (Fig. 6a–d). This seasonal cycle of the Costa Rica Dome is also depicted in RSM-ROMS (Fig. 7). However, RSM-ROMS displays a shallower thermocline depth and weaker surface ocean currents throughout the year over this region of the Pacific Ocean (Fig. 7). Furthermore, SODA reanalysis displays an

anticyclonic gyre between the Gulf of Papagayo and Gulf of Tehuantepec (GPTG) far more strongly in the winter months (Jan–Feb–Mar; Fig. 6) than in RSM-ROMS (Fig. 7). Perez et al. (2000) using two years of sea surface temperature data, remotely sensed altimetry, and scatterometer based wind stress datasets identified warm gyres forming in the winter months in this region. These gyres form because of the seasonal peak in strong off-shore low-level atmospheric gap winds in the Sierra Madre ranges that create anticyclonic wind stress curl producing warm core gyre in the region (Perez et al. 2000; Kessler 2006).

The bias of RSM-ROMS in the evolution of the Costa Rica Dome is also observed in the surface ocean currents. For example, the westward flowing SEC is much stronger and anchored closer to the equator in RSM-ROMS (Fig. 7) compared to SODA (Fig. 6) throughout the year. However, the seasonal cycle of eastward flowing NECC is far more reasonable in the RSM-ROMS simulation with its peak around 5°N in October and its nadir in March. The westward flowing NEC appears strong at ~10°N from January through April and then shifts further north and weakens slightly till October before the NEC begins to shift southward and strengthen (Fig. 6). The RSM-ROMS simulation in Fig. 7 shows a similar seasonal cycle of NEC as SODA reanalysis. Similarly, the seasonal peak of Costa Rica Counter

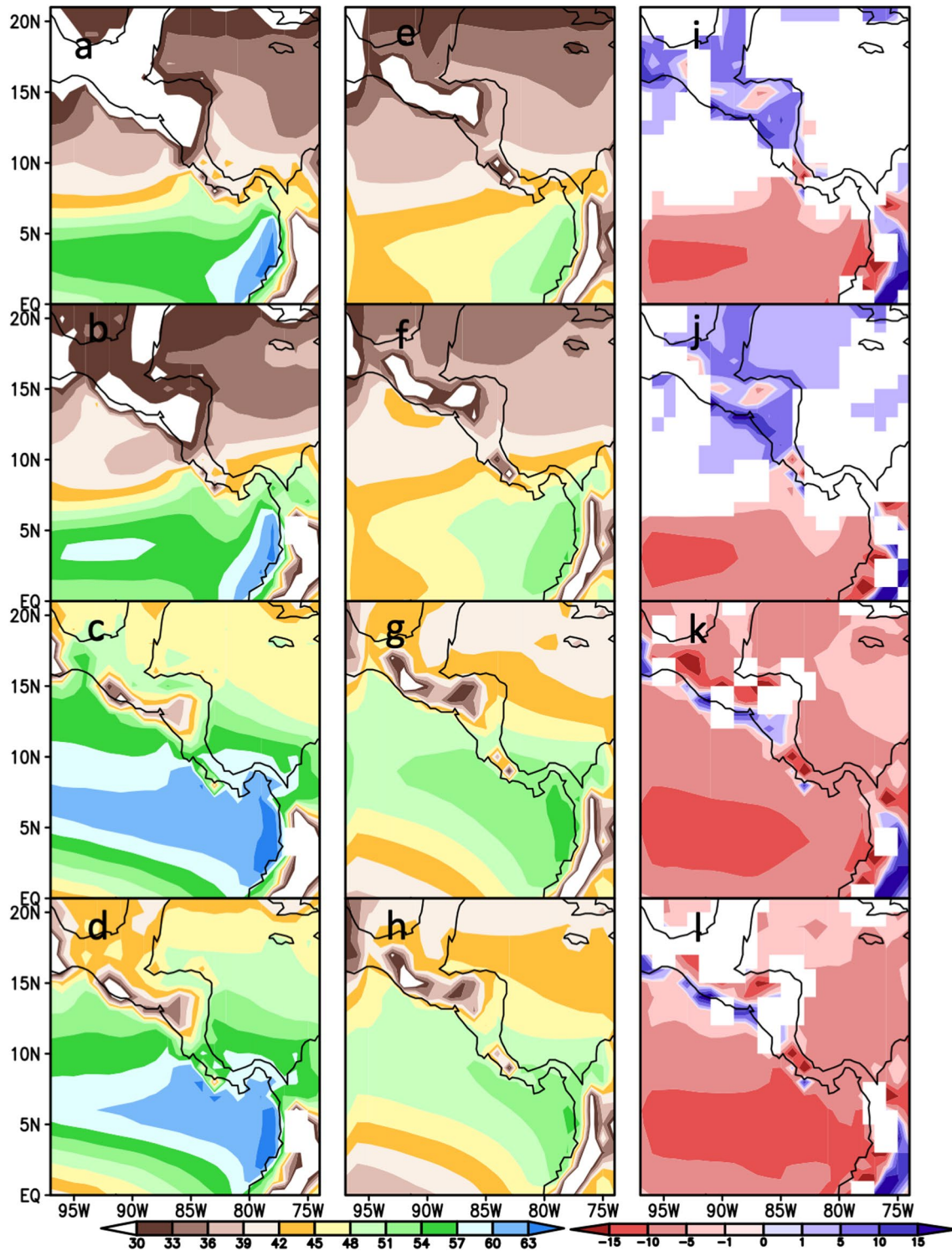


Fig. 4 The seasonal climatological precipitable water (Kgm^{-2} ; shaded), **a, b, c, d** observations (NVAP), and **e, f, g, h** RSM-ROMS for **a, e** December–January–February, **b, f** March–April–May, **c, g**

June–July–August, and **d, h** September–October–November seasons. The corresponding systematic errors (shaded only if they exceed 95% confidence interval) of RSM-ROMS is shown in (**i, j, k, and l**)

Current in JJA in SODA reanalysis (Fig. 6) is also simulated in RSM-ROMS (Fig. 7).

The upper ocean circulation in the Caribbean Sea is dominated by the Caribbean Current (Fig. 6). This is a warm, persistent surface current that flows along the northern

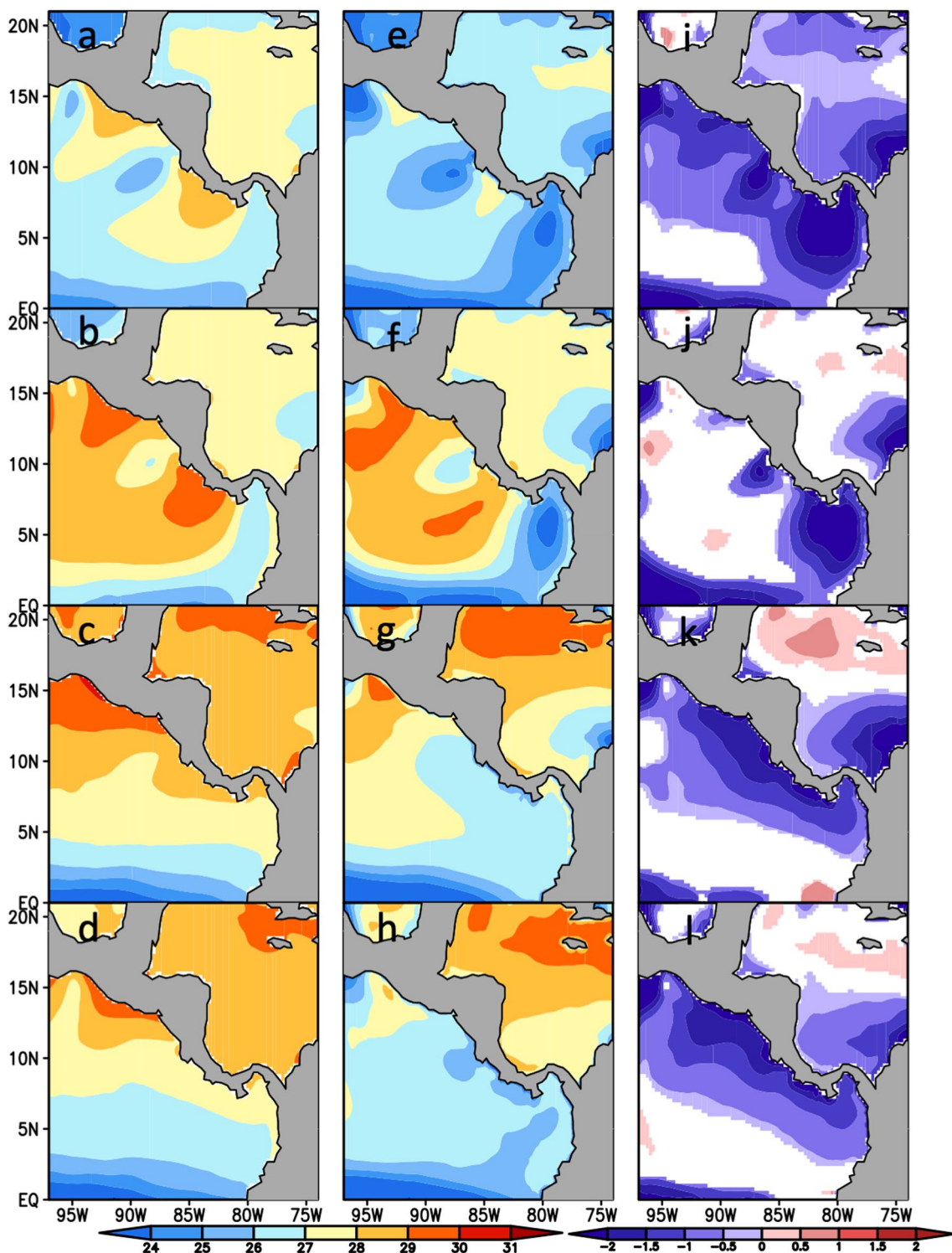


Fig. 5 The seasonal climatological SST (°C; shaded), **a, b, c, d** observations (NOAA OISSTv2), and **e, f, g, h** RSM-ROMS for **a, e** December–January–February, **b, f** March–April–May, **c, g** June–

July–August, and **d, h** September–October–November seasons. The corresponding systematic errors (shaded only if they exceed 95% confidence interval) of RSM-ROMS is shown in (**i, j, k, and l**)

coast of South America and then along the eastern coast of CAI. Another surface ocean feature of note in the Caribbean Sea is the highly variable Panama-Colombia Gyre over

the Colombian Basin. At the resolution of SODA reanalysis (at 0.5°), this gyre is barely resolved and is most apparent in July–August–September–October season (Fig. 6). The

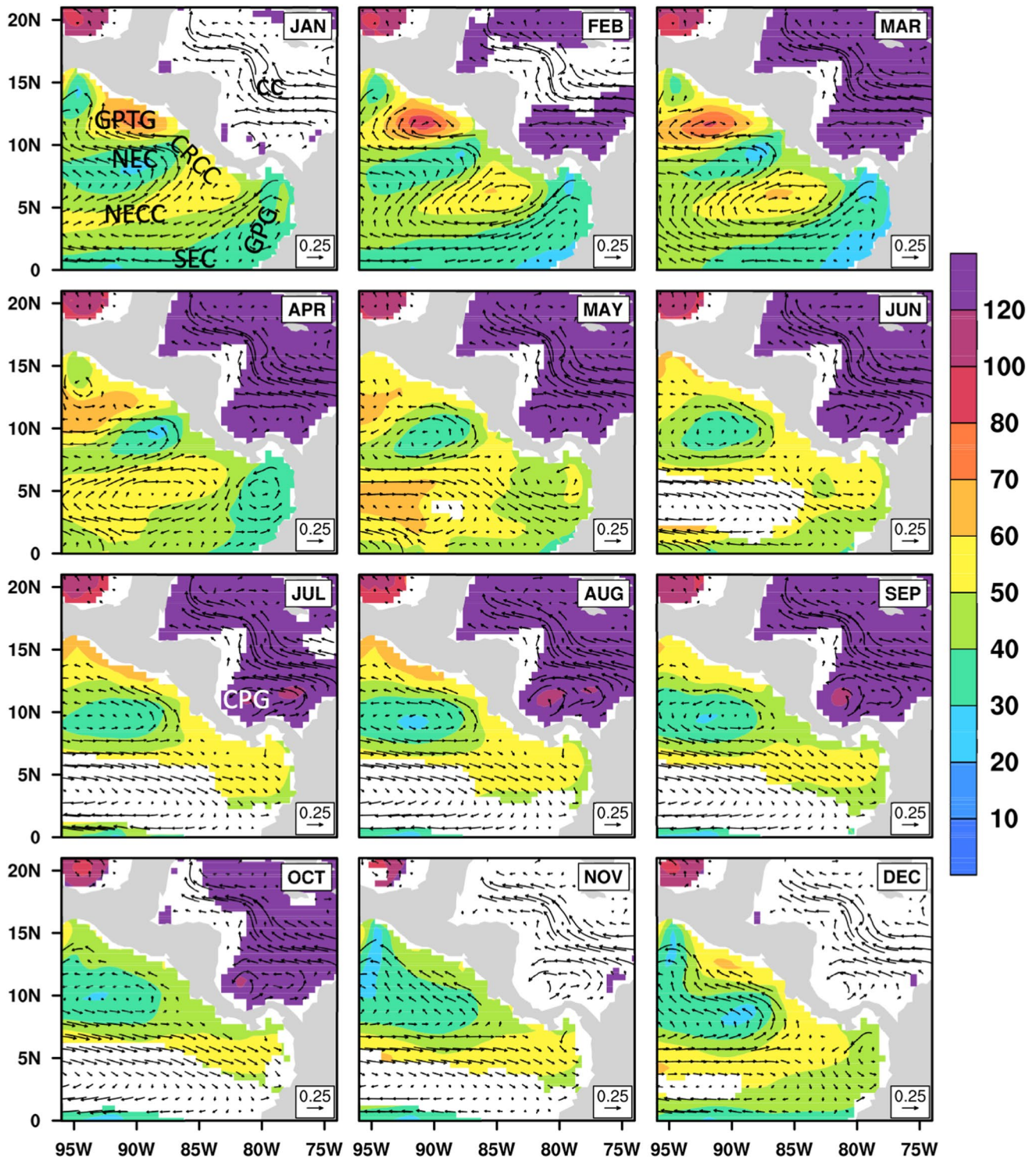


Fig. 6 The monthly mean climatology of the thermocline depth (measured as the depth of the 20 °C isotherm; m) overlaid with surface ocean currents (ms^{-1}) from SODA. The prominent surface ocean currents in the region like the westward flowing North Equatorial Current (NEC) and South Equatorial Current (SEC), eastward flowing North Equatorial Countercurrent (NECC), northwestward flow-

ing Costa Rica Coastal Current (CRCC), the Gulf of Panama Gyre (GPG), and the Gulf of Papagayo-Tehuantepec Gyre (GPTG) of the Pacific and the Caribbean Current (CC) in the Atlantic are identified in the first panel. The Colombia-Panama Gyre (CPG) is indicated in the third row, first column panel. The non-shaded areas mean that the thermocline depth is undefined

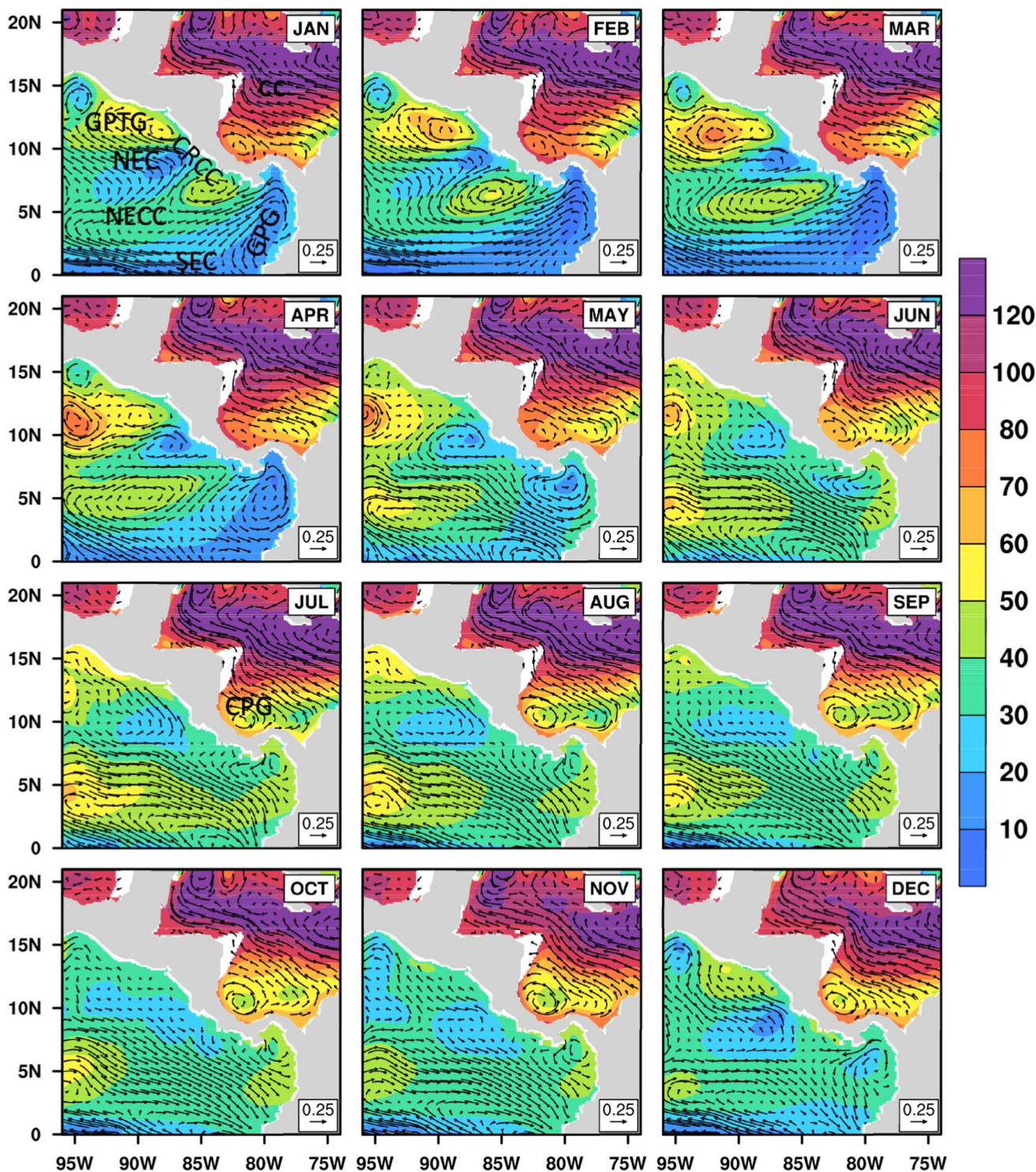


Fig. 7 The monthly mean climatology of the thermocline depth (measured as the depth of the 20 °C isotherm; m) overlaid with surface ocean currents from the RSM-ROMS simulation. The prominent surface ocean currents in the region like the westward flowing North Equatorial Current (NEC) and South Equatorial Current (SEC), eastward flowing North Equatorial Countercurrent (NECC), north-

westward flowing Costa Rica Coastal Current (CRCC), the Gulf of Panama Gyre (GPG), and the Gulf of Papagayo-Tehuantepec Gyre (GPTG) of the Pacific and the Caribbean Current (CC) in the Atlantic are identified in the first panel. The Colombia-Panama Gyre (CPG) is indicated in the third row, first column panel. The non-shaded areas mean that the thermocline depth is undefined

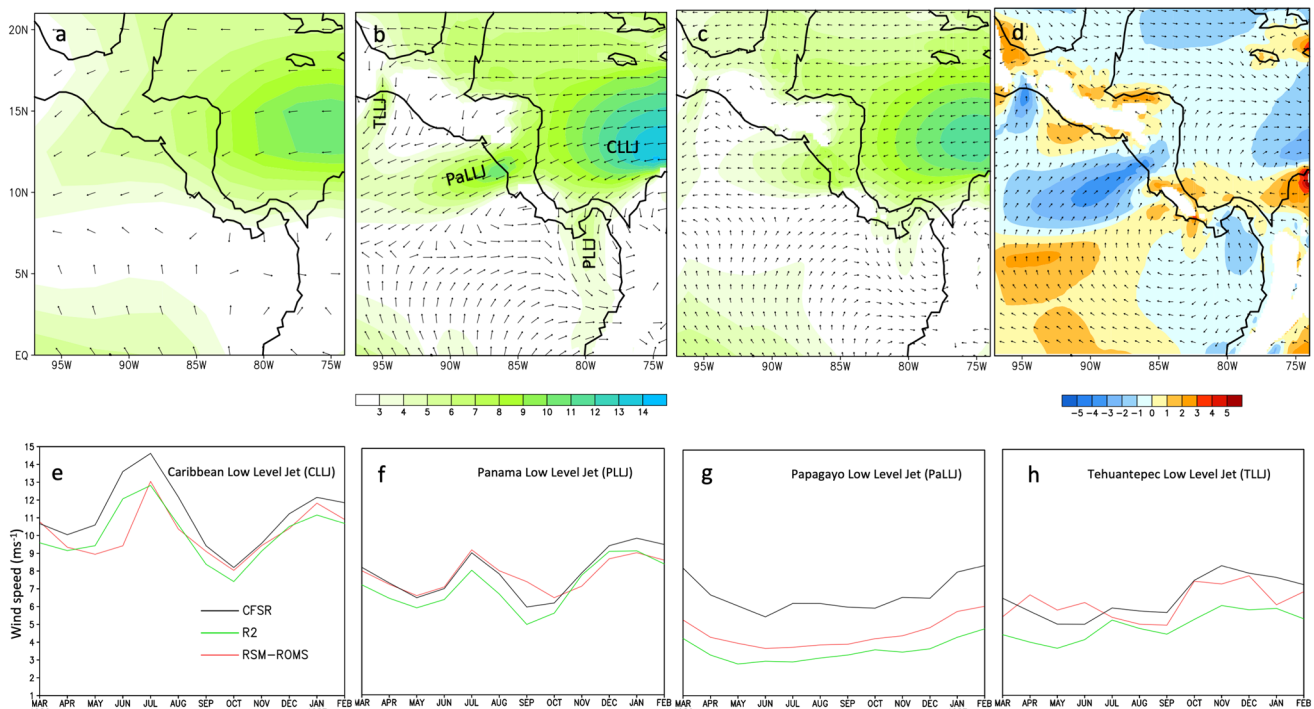


Fig. 8 The climatological annual mean 925 hPa winds from **a** R2, **b** CFSR, **c** RSM-ROMS, and **d** corresponding difference between RSM-ROMS and CFSR (**c–b**). The seasonal cycle of the magnitude of the 925 hPa winds (ms^{-1}) for **e** Caribbean LLJ index (CLLJ; averaged over 12.5°N – 17.5°N and 76°W – 80°W), **f** Panama LLJ index

(PLLJ; averaged over 3°N – 8°N and 76°W – 80°W), **g** Papagayo LLJ index (PaLLJ; averaged over 11°N – 14°N and 82°W – 90°W), and **h** Tehuantepec LLJ index (TLLJ; averaged over 13°N – 18°N and 94°W – 96°W). The shaded values in (**a–d**) is the magnitude (ms^{-1}) of the wind vectors

climatological surface ocean circulation in RSM-ROMS in Fig. 7 shows the persistent Caribbean Current in the northern Colombian Basin, western Cayman and Yucatan Basin and a rather strong cyclonic recirculation associated with Panama-Colombian Gyre in southwestern Caribbean Sea. The seasonal variation of the Panama-Colombian Gyre in RSM-ROMS with intense cyclone in the boreal winter months to multiple cyclones of similar size embedded in a larger but weaker cyclonic circulation in the Caribbean Sea is in qualitative agreement with previous observational findings (Andrade and Barton 2000; Fratantoni 2001). The depth of the thermocline in the Caribbean Sea is, however, consistently shallower in RSM-ROMS (Fig. 7) compared to that in SODA reanalysis (Fig. 6). The cold SST bias of RSM-ROMS along the coastal oceans of CAI (Figs. 5i–l), combined with the corresponding bias of shallower thermocline depth (comparing Fig. 7 with Fig. 6), especially in the summer and fall seasons along the coastal ocean suggests that the upper ocean is highly stratified in RSM-ROMS. In other words, RSM-ROMS could benefit from stronger mixing in the upper ocean to reduce some of its bias in both these coastal oceans of CAI.

4.4 The seasonal cycle of the low level jets

One of the grand challenges of modeling the climate of this region are the multitude of LLJs that have significant implication on the hydroclimate of the region. In this regard, the regional domain of the RSM-ROMS includes four prominent LLJs: The Caribbean Low Level Jet (CLLJ), the Panama Low Level Jet (PLLJ), the Papagayo Low Level Jet (PaLLJ), and the Tehuantepec Low Level Jet (TLLJ). The LLJs are represented by their indices obtained by area averaging the monthly mean winds over 12.5°N – 17.5°N and 76°W – 80°W for CLLJ, over 3°N – 8°N and 76°W – 80°W for PLLJ, over 11°N – 14°N and 82°W – 90°W for PaLLJ, and over 13°N – 18°N and 94°W – 96°W for TLLJ. The climatology of the 925 hPa wind field created from both the CFSR and the RSM-ROMS integration are shown in Fig. 8. We will discuss the winds from R2 shown in Fig. 8 in Sub-section g. All these LLJs are apparent in the CFSR annual mean climatology of the 925 hPa wind from their distinct maxima in the wind speed (Fig. 8b). The annual mean 925 hPa winds from RSM-ROMS (Fig. 8c) and its corresponding systematic errors in Fig. 8d show that the RSM-ROMS clearly underestimate all these LLJs relative to CFSR. In contrast to the annual mean climatology of the 925 hPa winds of the RSM-ROMS simulation, the seasonal simulation of the LLJs in the

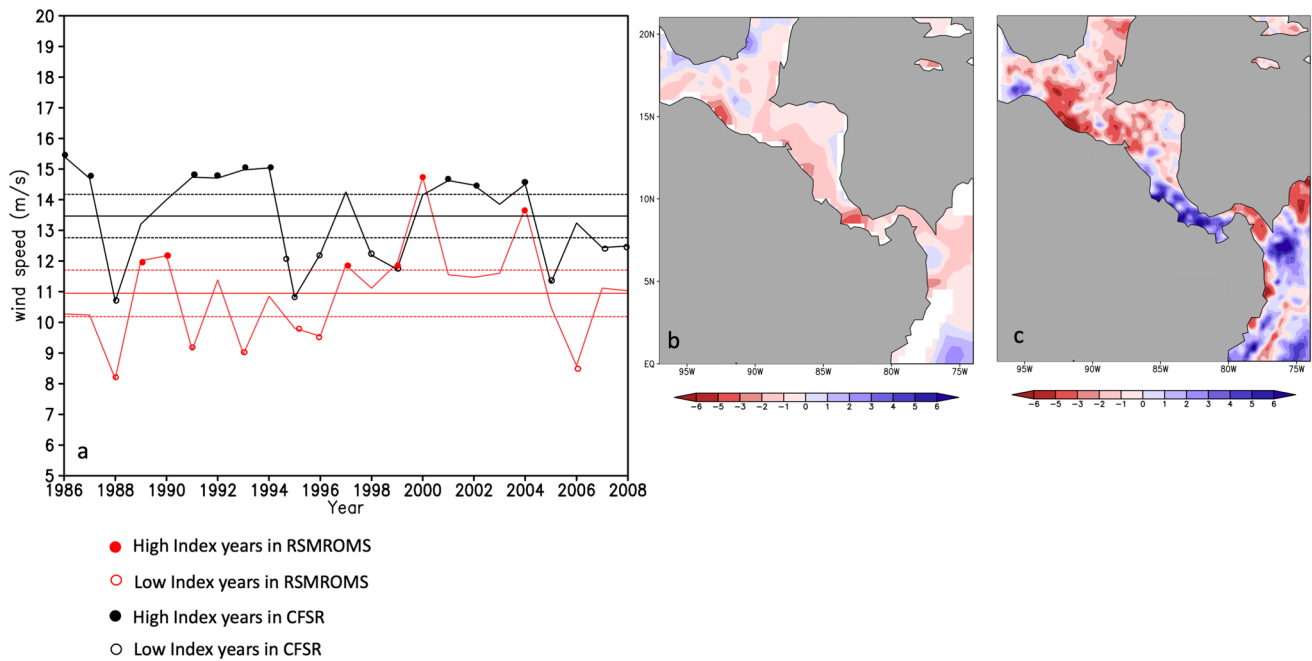


Fig. 9 **a** The Caribbean Low Level Jet (CLLJ) index for JJA from CFSR (black line) and RSM-ROMS (red line). The open and filled circles indicate high and low CLLJ index seasons. The solid horizontal lines are the corresponding mean of the CLLJ index from CFSR (black) and RSM-ROMS (red). The dotted horizontal lines on either side of the mean is (mean $\pm 0.75 \times$ standard deviation) of the CLLJ

index from CFSR (black) and RSM-ROMS (red). The corresponding difference of seasonal mean rainfall (mm day^{-1}) between high and low CLLJ index years for JJA from **b** CPC and **c** RSM-ROMS. Only significant values at 95% confidence interval according to *t*-test in (**b**, and **c**) is plotted

RSM-ROMS simulation is reasonable (Fig. 8e–h) besides the significant underestimation of the magnitude of the PaLLJ throughout the year (Fig. 8c). For example, the dual maximum of the CLLJ with primary and secondary peak in the boreal summer and winter is reasonably captured by the RSM-ROMS simulation (Fig. 8e). Likewise, the CFSR shows PLLJ with a dual maximum, with primary peak in January and secondary peak in July (Fig. 8f). However, the RSM-ROMS can simulate the dual maximum in PLLJ, it shifts the primary peak to July and secondary peak in January (Fig. 8f). PaLLJ in Fig. 8g, shows that it peaks in February–March in CFSR, which the RSM-ROMS can simulate reasonably with underestimation of its magnitude throughout the year. CFSR indicates that the TLLJ reaches its annual peak in November with significant month-to-month variability (Fig. 8h). The TLLJ are more commonly observed during the boreal winter months and during warm, El Niño years (Romero-Centeno et al. 2003), which supports the seasonal cycle of TLLJ shown in Fig. 8h. The RSM-ROMS shows the seasonal cycle of TLLJ peaking in October and December with a slight dip in its magnitude in November (Fig. 8h).

4.5 Interannual variability

The interannual variations of precipitation in CAI is largely dictated by the variability of the LLJs (Duran-Quesada et al. 2017). Amongst the LLJs, the interannual variations of the CLLJ during the JJA season dictate to a large extent the interannual variability of the summer hydroclimate over CAI (Wang et al. 2007, 2008; Misra et al. 2014). This variation of the CLLJ is associated with the variations of the Atlantic warm pool in the IAS (Wang et al. 2007, 2008), the variations of the meridional pressure gradient across the Caribbean Basin modulated by the tropical Pacific variability (Munoz et al. 2008) and the zonal gradient of SST between the tropical Atlantic and eastern Pacific Oceans (Enfield and Alfaro 1999). In the winter although, CLLJ has a seasonal peak, it does not serve as large of a source of moisture to CAI as in the summer, since the associated moisture flux vectors are comparatively weaker (Munoz et al. 2008). Furthermore, Maldonado et al. (2018) suggest that in the winter, moisture convergence in CAI is less important to dictate the hydroclimate than during the rest of the year. In Fig. 9a we show the timeseries of the CLLJ index from CFSR and RSM-ROMS for the JJA season. The years of high and low CLLJ index are highlighted in Fig. 8a. These high and low index seasons are chosen if the CLLJ index exceeds or is

less than the corresponding seasonal climatological mean for JJA by $0.5 \times$ standard deviation, respectively. The fractional coefficient of 0.5 was chosen to achieve reasonable sample of seasons for high and low index seasons to conduct a meaningful statistical significance test on the corresponding precipitation anomalies computed from the composite difference between the high and low CLLJ index years. The CLLJ index in JJA season shows far higher interannual variability in RSM-ROMS than CFSR (Fig. 8a). The variations of the timeseries of the CLLJ index between CFSR and RSM-ROMS in Fig. 8a are understandably inconsistent with each other (meaning high and low index years are not coinciding between CFSR and RSM-ROMS) for several reasons. These include the notion that climate simulation is not an initial value problem, contributions of the bias (e.g., in SST, sea level pressure gradients that dictate the variability of low-level winds) and from the internal variability in RSM-ROMS. Furthermore, the bias and variations in the R2 reanalysis that is forcing the RSM-ROMS may also contribute to the inconsistencies in the variations of the CLLJ in the RSM-ROMS simulation (Fig. 8a).

The composite difference of JJA seasonal mean rainfall between the high and the low CLLJ index years shown in Fig. 8b from CPC rainfall indicate that most of CAI has a dry anomaly, consistent with the moisture flowing across the CAI into eastern Pacific to feed the ITCZ when the CLLJ is comparatively strong (Wang et al. 2007; Misra et al. 2014; Duran-Quesada et al. 2017; Corrales-Suastegui et al. 2020). It may be noted that we use land based CPC rainfall for this comparison because the period of this rainfall dataset overlaps with that of CFSR and RSM-ROMS simulation. The RSM-ROMS simulation in Fig. 8c shows similar seasonal mean rainfall anomalies as the observations (Fig. 8b) over Guatemala, southern Mexico, Nicaragua, Honduras, and Costa Rica. However, the positive rainfall anomalies in RSM-ROMS over Panama and northeast Colombia in Fig. 8c are unsubstantiated in the observations (Fig. 8b).

4.6 The mid-summer drought

The iconic feature of the region is the mid-summer drought (Magana et al. 1999). This was diagnosed both in the observations and in RSM-ROMS when a relative minimum of rainfall in July and August, was observed between biannual peaks in June and September (Fig. 3b). We defined intensity of the mid-summer drought as the difference between the average of the biannual peak and the average of the minimum in the intervening two months (Fig. 10a, b). Their frequency of occurrence is identified in Fig. 10c, d as fraction of seasons with mid-summer drought in the 25 years (1986–2010).

The observations show that the Yucatan region and the Pacific side of the northern part of the CAI (e.g., western

coasts of Southern Mexico and Guatemala, Nicaragua, and San Salvador) exhibit largest intensity (Fig. 10a) and highest frequency (Fig. 10c) of the mid-summer drought. South of Nicaragua, the frequency of the mid-summer drought drops significantly (Fig. 10c) while the intensity over Costa Rica and Panama are moderate (Fig. 10a). The western coast of Colombia displays high frequency (Fig. 10c), but the intensity is low (Fig. 10a). The RSM-ROMS simulation shows some of these features, like high intensity in the Yucatan Peninsula, western coasts of Southern Mexico, Guatemala, Nicaragua, and San Salvador. However, the intensity is overestimated by RSM-ROMS and extends the high intensity mid-summer drought across to Costa Rica, and Panama (Fig. 10b). Furthermore, RSM-ROMS clearly overestimates the frequency of the mid-summer drought over the Yucatan Peninsula, although the frequency along the western coast of the high intensity region is reasonable (Fig. 10d).

4.7 Tropical cyclone activity

The Tropical Cyclone (TC) activity is shown as track density (which is number of TCs per $1^\circ \times 1^\circ$ grid) in Fig. 11. As noted earlier, Fig. 11 plots the TC fix at six-hour interval over the integration period of 1986–2010. RSM-ROMS (Fig. 11b) shows reasonable distribution of the TCs in comparison to HURDAT2 (Fig. 11a) both over the Caribbean Sea and the eastern Pacific with some notable biases. Some highlights of the RSM-ROMS simulation is, it does not generate TCs below 6.5°N in the eastern Pacific like HURDAT2. The distribution of the TCs in the Caribbean Sea with a cluster of high density between the Cayman and Yucatan Basins and over the Nicaraguan Rise in RSM-ROMS (Fig. 11b) compares well with HURDAT2 (Fig. 11a). However, the biases displayed by RSM-ROMS include the relatively larger density of TCs in the Colombian Basin, tropical northeastern Pacific and between Cayman and Yucatan Basins (Fig. 11b) is unsupported by HURDAT2 (Fig. 11a). As a result, the contrast of the greater number of TCs in the Caribbean Sea than over the eastern Pacific in HURDAT2 (Fig. 11a) is less prominent in the RSM-ROMS simulation (Fig. 11b).

4.8 Comparison with R2

The key benefit of dynamic downscaling is its ability to resolve or permit the fine scale features of the regional climate because of the superior horizontal resolution of the regional model. This feature of downscaling in our study has thus far been fairly demonstrated in the fidelity of RSM-ROMS in depicting some mesoscale features like the Costa Rica Dome, the Panama-Colombian and the Papagayo-Tehuantepec Gyres, the atmospheric LLJs, interannual and sub-seasonal variations of rainfall over Central America and the TC activity in the region. The other value of dynamic

Fig. 10 The **a, b** intensity (I ; units: mm day^{-1}) and **c, d** frequency (F ; fraction of events in 25 years: 1986–2010) of the mid-summer drought events from **a, c** CPC and **b, d** RSM-ROMS simulation

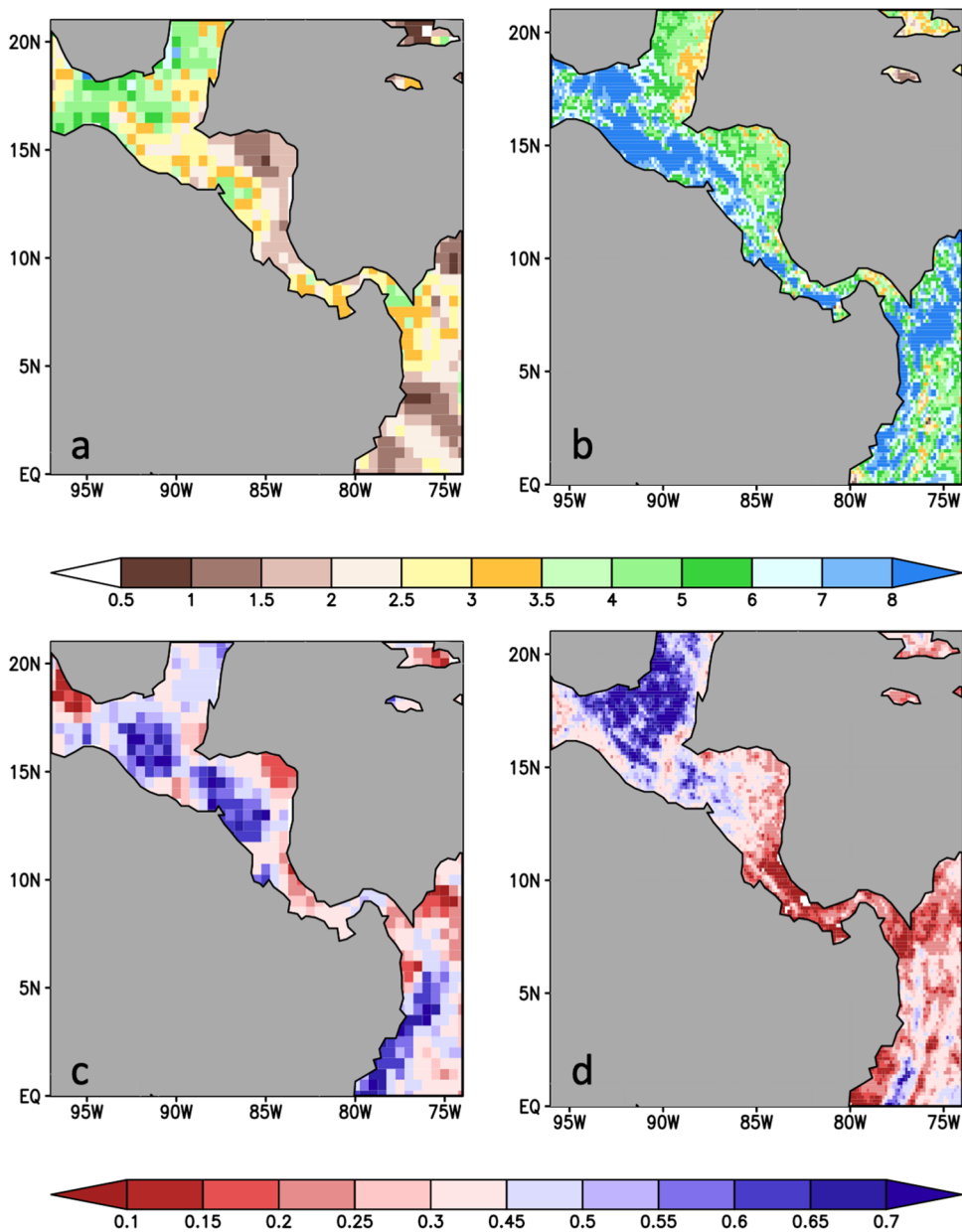


Fig. 11 The track density plot of the TCs (i.e., number of TCs per $1^\circ \times 1^\circ$) from **a** HURDAT2 and **b** RSM-ROMS simulation over the time period of 1986–2010. It may be noted that the track density is based on once-a-day tracking data for both panels. The tracking algorithm used in **(b)** follows from Ullrich and Zarzycki (2017)

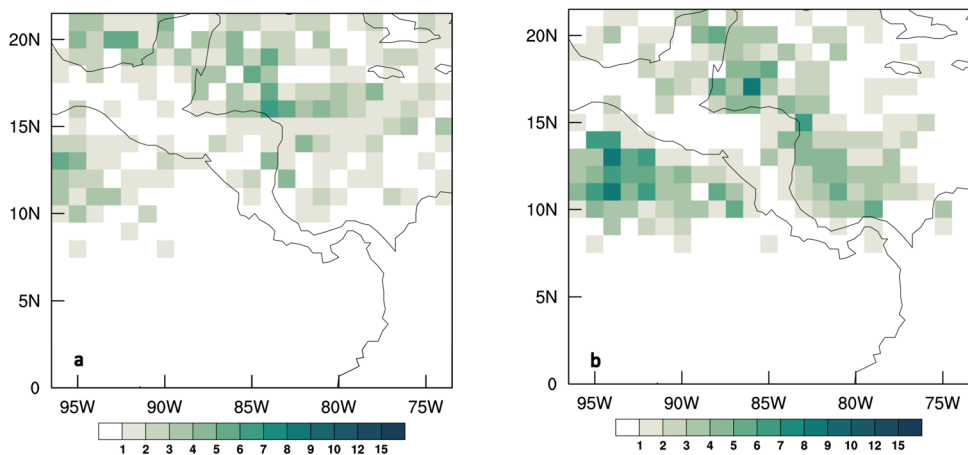
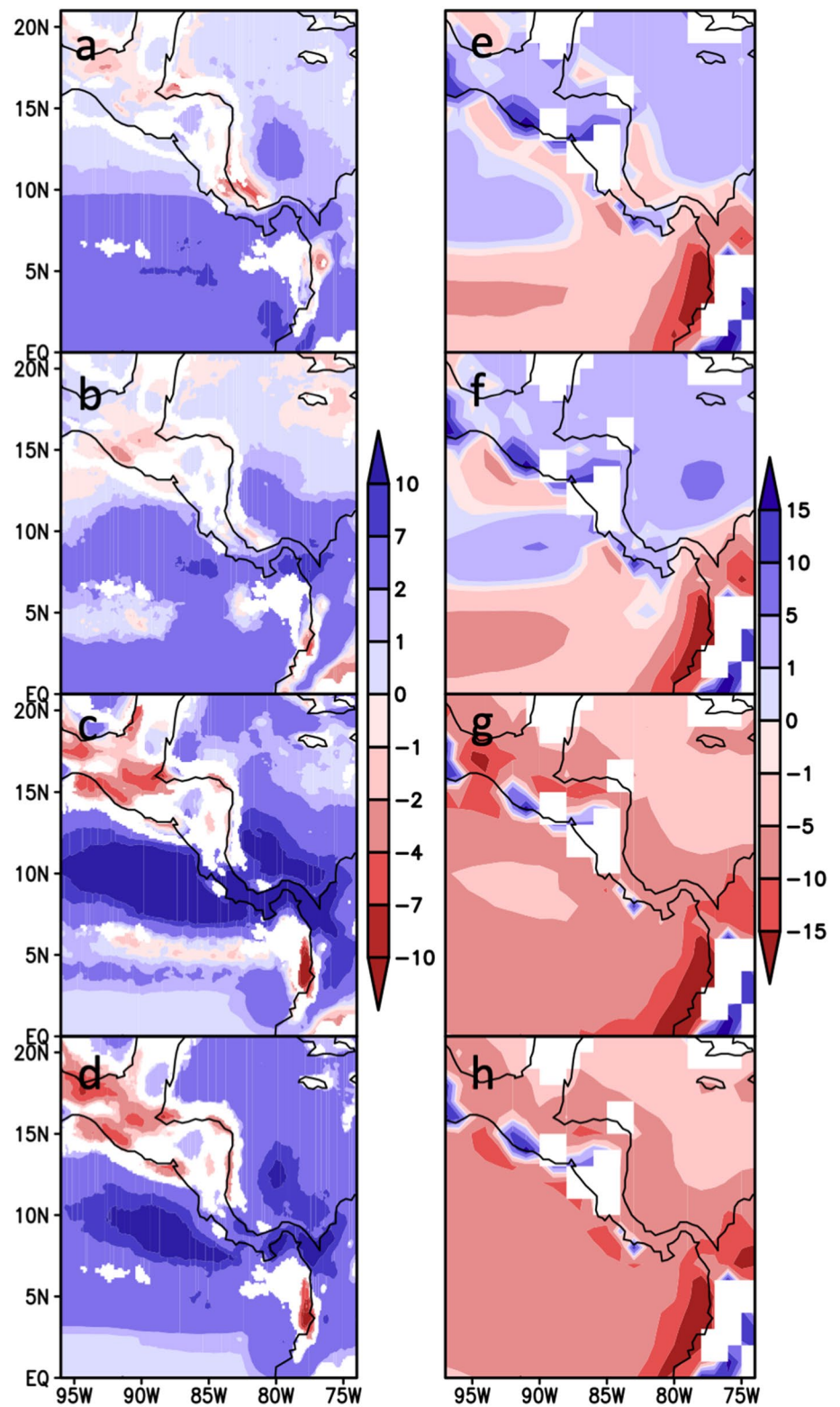


Fig. 12 The seasonal mean climatological error of **a–d** rainfall (mm day^{-1}) and **e–h** precipitable water (kgm^{-2}) from R2 reanalysis used in the lateral boundary forcing of RSM-ROMS for **a, e** DJF, **b, f** MAM, **c, g** JJA, and **d, h** SON. The observations for rainfall and precipitable water are IMERG and NVAP, respectively



downscaling is its potential to improve upon the large-scale forcing used to force the regional model. Therefore, in our case it would be incumbent to compare the systematic errors of R2 reanalysis with those from RSM-ROMS. It may

however be added, that RSM-ROMS by way of its coupled ocean–atmosphere framework already adds value to downscaling in contrast to either R2 or SODA reanalysis, which

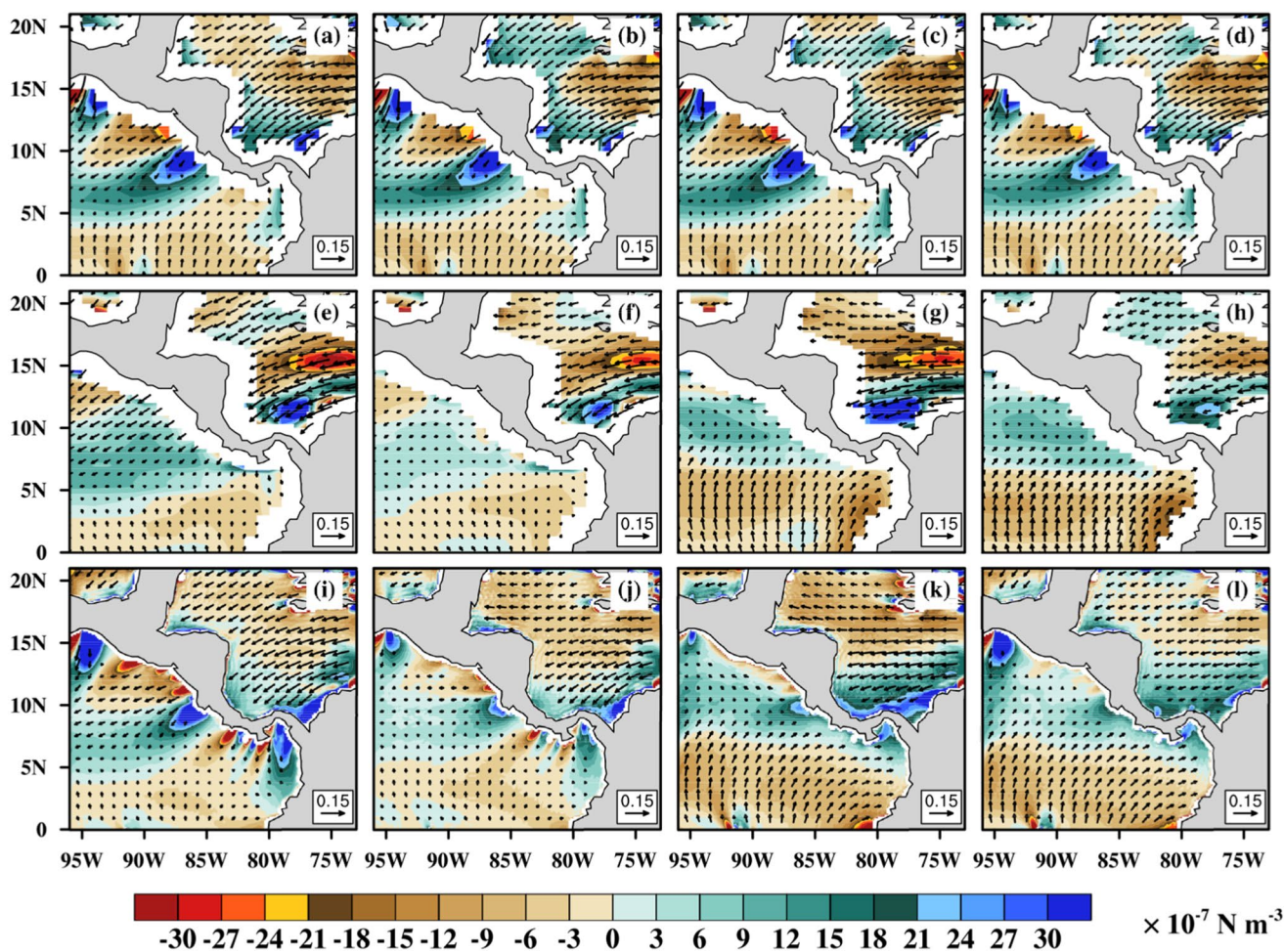


Fig. 13 The seasonal mean climatology of wind stress (Nm^{-2} ; vectors) and the curl of the wind stress (Nm^{-3} ; shaded) from **a–d** observations, **e–h** R2 reanalysis, and **i–l** RSM-ROMS simulation for **a, e, i** DJF, **b, f, j** MAM, **c, g, k** JJA, and **d, h, l** SON seasons

are exclusively global atmospheric or oceanic reanalysis, respectively.

In Fig. 12a–d, we show the systematic errors of seasonal mean rainfall from R2. In comparison to RSM-ROMS (Fig. 2i–l), the systematic errors of R2 (Figs. 3a–c, 12a–d) are far higher over the oceans and far less over the CAI. An interesting point, however, is that the systematic errors of rainfall in the tropical eastern Pacific Ocean over the location of the ITCZ ($\sim 5^\circ\text{N}$) is exacerbated in RSM-ROMS relative to R2 except in the winter season. This may be a result of the air–sea coupling in RSM-ROMS being more active in tropical eastern Pacific Ocean that allows for more degrees of freedom, with the ocean co-evolving with the atmosphere. On the other hand, the systematic errors display significant reduction of the wet bias over the Caribbean Sea in RSM-ROMS relative to R2 (Figs. 2i–l, 3c, 12a–d).

The comparison of the systematic errors of precipitable water between R2 (Fig. 12e–h) and RSM-ROMS (Fig. 4i–l) indicate that they are comparable to each other (Fig. 3d–f).

It is apparent from this comparison that the systematic errors in precipitable water are far more consistent in RSM-ROMS in relation to R2, which contrasts with the systematic errors of rainfall. This is because specific humidity is one of the prescribed variables at the lateral boundaries of RSM-ROMS and hence the evolution of humidity is constrained to that imposed at the lateral boundaries. However, rainfall is not constrained by the lateral boundaries of RSM-ROMS, especially over the oceans where air–sea coupling is likely playing a significant role. The worsening of the rainfall and precipitable water bias over land in RSM-ROMS relative to R2 (Fig. 3b), however is surprising but also could be attributed to the fine scale resolution of the orography, which is often the ‘Achilles heel’ of spectral models (Yorgun and Rood 2014).

The comparison of the low-level winds at 925 hPa in Fig. 8 reveals that despite the coarse resolution of R2, the LLJs are reasonably depicted including their seasonal cycle. The RSM-ROMS in most instance replicates this seasonal

cycle of the LLJs in R2 and CFSR. In all instances of the four LLJs, the RSM-ROMS seems to be a slight improvement over R2 in relation to CFSR (Fig. 8e–h).

One of the important forcing to the ocean is the surface wind stress, which is demonstrably significant for the mesoscale variations of the surface ocean currents in the region (Fiedler 2002; Sheng and Tang 2003). The easterly wind stress in the Caribbean Sea and in the northeastern Pacific Ocean are dominant both in the CFSR and in RSM-ROMS (Fig. 13). Similarly, southerly and northeasterly wind stress over the equatorial eastern Pacific Ocean and over the Colombian Basin, respectively is also apparent in Fig. 13. Similarly, the wind stress curl shows regions of strong upwelling and downwelling in both oceans that have distinct seasonality associated with the Costa Rica Dome, ITCZ in the eastern Pacific, and the LLJs (Fig. 12). There are however subtle differences between R2 (Fig. 13e–h) and RSM-ROMS (Fig. 13i–l). For example, the upwelling associated with Costa Rican Dome in the tropical eastern Pacific Ocean and Panama-Colombia Gyre in the Caribbean Sea is stronger in RSM-ROMS (and closer to CFSR in Fig. 13a–d) compared to R2 (Fig. 13e–h).

The Pacific coast of CAI is dominated by the tropical eastern Pacific warm pool that extends from late March through mid-August (Misra et al. 2016). This stratification of the warm pool breaks down in the boreal winter by the action of the NASH that extends over the Gulf of Mexico across the north Atlantic (Misra 2020) that induce strong LLJs (viz., PLLJ, PaLLJ, TLLJ) that pass through the cordillera of the CAI (Fig. 8f–h). In the case of all three of these LLJs the altitude of the CAI is sufficiently low, so that the PLLJ, PaLLJ, and TLLJ are sufficiently intense and remain at low enough altitude to push the surface waters away from the Pacific coast of CAI. As a result, deeper, colder, and nutrient rich water are upwelled to replace this expelled surface water from the Pacific coast of CAI (Legeckis 1988; McCreary et al. 1989). This process of wind-jet driven seasonal upwelling is apparent in CFSR (Fig. 13a–d) and RSM-ROMS simulation (Fig. 13i–l) in the Gulf of Tehuantepec, Gulf of Papagayo, and the Gulf Panama. Furthermore, the upwelling associated with these LLJs are seasonal from the seasonality of the LLJ and the meridional movement of the ITCZ. The duration of the upwelling also becomes progressively shorter as one travels south from the Gulf of Tehuantepec (where it can persist up to eight months) to Gulf of Panama (where it persists up to 3 months in the boreal winter; D’Croz and O’Dea 2007). These seasonal cycles of the upwelling associated with the LLJs are clearly observed in the RSM-ROMS simulation (Fig. 13i–l), which is not so apparent in even CFSR (Fig. 13a–d). In contrast, the R2 reanalysis shows weak upwelling in the Gulf of Papagayo and is unable to resolve upwelling in the Gulf of Tehuantepec and the Gulf of Panama.

5 Conclusions

In this study we have examined the fidelity of an multi-decadal regional coupled ocean–atmosphere model (RSM-ROMS) simulation over Central America at an unprecedented 15 km grid spacing. The last such regional coupled ocean-model atmosphere modeling study over the region was conducted by Cabos et al. (2019), which was conducted at 25 km and 50 km grid spacing in two separate integrations. The CAI, by its geography has a very rich amalgam of variations that feature both the surrounding oceans and over the land surface, which warrants the use of such relatively high resolution coupled ocean–atmosphere models. The current state-of-the-art global climate models at a nominal spatial resolution ranging between 2° and 1° are highly inadequate for either simulating or projecting future climate over the CAI region.

The highlights of the RSM-ROMS simulation over the CAI region, forced with R2 global atmospheric reanalysis and SODA ocean reanalysis at the lateral boundaries are as follows:

- The seasonal cycle of precipitation over CAI and the surrounding oceans is reasonable. Both R2 and RSM-ROMS integration show the phenomenon of the mid-summer drought clearly in the climatological seasonal cycle of precipitation over CAI. The RSM-ROMS displays significant improvement over R2 over the oceans (tropical eastern Pacific Ocean and the Caribbean Sea) suggesting the potential role of air-sea coupling. But the climatological errors of precipitation over CAI suggest a severe wet bias in RSM-ROMS that is far more than in R2. However, the differences in the rain gauge based CPC rainfall analysis and satellite based IMERG rainfall analysis is also significantly large over CAI, suggesting observational uncertainties.
- The seasonal cycle of precipitable water clearly shows the meridional gradient of high precipitable water over the equatorial latitudes to lower precipitable water in the subtropics throughout the year in both observations (CFSR) and RSM-ROMS simulation. However, the systematic errors in simulated precipitable water suggesting a drier atmospheric column across the domain by RSM-ROMS is very similar to those in R2, suggesting the strong influence of the lateral boundary conditions on the simulation.
- The seasonal cycle of the equatorial Pacific cold tongue and the western hemisphere warm pool in RSM-ROMS is validated with corresponding seasonal cycle in OIS-STv2. However, RSM-ROMS displays a severe cold bias along the coastal waters of CAI because of stronger stratification of the upper ocean and a shallower thermocline

than SODA reanalysis. The RSM-ROMS simulation of the anticyclonic Gulf of Papagayo-Tehuantepec gyre is also found to be reasonable. Because of the high resolution of RSM-ROMS, the Panama-Colombia gyre over the Colombian Basin is resolved.

- The seasonal cycle of the four LLJs (CLLJ, PLLJ, PaLLJ, and TLLJ) in the RSM-ROMS simulation follow those in R2 and is reasonably similar to CFSR. The magnitudes of these LLJs in RSM-ROMS show a modest improvement over R2 relative to CFSR. The wind jet driven upwelling in the RSM-ROMS simulation the Gulfs of Tehuantepec, Papagayo, and Panama are also verified with observations (CFSR).
- The interannual variations of the CLLJ in the summertime show verifiable precipitation response over the northern part CAI (e.g., Yucatan Peninsula, Honduras, Guatemala, El Salvador) in the RSM-ROMS simulation. In these regions stronger or weaker CLLJ in JJA season is associated with corresponding drier or wetter seasonal precipitation anomalies.
- The iconic feature of the mid-summer drought of the CAI in the RSM-ROMS simulation verifies in intensity and frequency in some areas like the Yucatan Peninsula, western coasts of Southern Mexico, Guatemala, Nicaragua, and San Salvador. However, the intensity is overestimated by RSM-ROMS and extends the high intensity mid-summer drought across to Costa Rica, and Panama. Furthermore, RSM-ROMS clearly overestimates the frequency of the mid-summer drought over the Yucatan Peninsula.
- The track density of the TCs in RSM-ROMS shows some important observed features like a cluster of high density TCs between the Cayman and Yucatan Basins and over the Nicaraguan Rise and there are no TCs generated south of 6.5°N in the eastern Pacific. But the observed contrast of the greater number of TCs in the Caribbean Sea than over the eastern Pacific is less prominent in the RSM-ROMS simulation.

Despite these highlights, there is significant room for improving the RSM-ROMS simulation. The systematic errors of wet bias over CAI, underestimation of the magnitude of the LLJs, the underestimation of the thermocline depth, the strong influence of the lateral boundary condition bias on the precipitable water bias, and some erroneous spatial distribution of the intensity and frequency of the mid-summer drought are most apparent. These issues have to be further explored by examining parameterizations in the RSM-ROMS concerning processes like ocean mixing, atmospheric convection, gravity wave drag, and planetary boundary layer. However, the expectation to rectify the large-scale bias of the lateral boundary conditions by regional models like RSM-ROMS may be ambitious

and beyond what regional models are capable of (Giorgi et al. 2019).

Author contributions Corresponding author contributed to the study conception and design. Material preparation, data collection and analysis were equally done by VM and CBJ. All authors have read and approved the final manuscript.

Funding No funds, grants, or other support was received for conducting this study.

Data availability The authors are willing to share the data from the model upon request.

Declarations

Conflict of interest None.

Ethical approval COPE guidelines have been followed.

Consent to participate Not applicable.

References

- Afonso OC (2011) Natural disasters and migration: storms in Central America and the Caribbean and immigration to the U.S. UC Davis Undergrad. Res J 14: 1–18. <http://explorations.ucdavis.edu/docs/2011/andrade.pdf>.
- Alpert J, Kanamitsu M, Caplan P, Sela J, White G (1988) Mountain induced gravity wave drag parameterization in the NMC medium-range forecast model. In: Conference on Numerical Weather Prediction, 8th, Baltimore, MD. 726–733.
- Amador JA, Magaña VO (1999) Dynamics of the low level jet over the Caribbean, in 23rd conference on Hurricanes and Tropical Meteorology, Am Meteorol Soc, Dallas, Texas, pp. 868–869
- Amador JA, Durán-Quesada AM, Rivera ER, Mora G, Sáenz F, Calderón B, Mora N (2016) The easternmost tropical Pacific. Part II: seasonal and intraseasonal modes of atmospheric variability. *Revista de Biología Tropical* 64(1): S23–S57.
- Andrade CA, Barton ED (2000) Eddy development and motion in the Caribbean Sea. *J Geophys Res* 105:26191–26201
- Behrangi A et al (2014) Satellite-based precipitation estimation and its application for streamflow prediction over mountainous western US basins. *J Appl Meteorol Climatol* 53:2823–2842
- Cabos W, Sein DV, Durán-Quesada A, Liguori G, Koldunov NV, Martínez-López B, Alvarez F, Sieck K, Limareva N, Pinto JG (2019) Dynamical downscaling of historical climate over CORDEX Central America domain with a regionally coupled atmosphere-ocean model. *Clim Dyn* 52:4305–4328
- Carton JA, Giese BS (2008) A reanalysis of ocean climate using simple ocean data assimilation (SODA). *Mon Wea Rev* 136:2999–3017. <https://doi.org/10.1175/2007MWR1978.1>
- Cavazos T, Luna-Nino R, Cerezo-Mota R, Fuentes-Franco R, Mendez M, Martinez LFP, Valenzuela E (2020) Climatic trends and regional climate models intercomparison over the CORDEX-CAM (Central America, Caribbean, and Mexico) domain. *Int J Climatol*. <https://doi.org/10.1002/joc.6276>
- Chen M, Shi W, Xie P, Silva VBS, Kousky VE, Wayne Higgins R, Janowiak JE (2008) Assessing objective techniques for

- gauge-based analyses of global daily precipitation. *J Geophys Res* 113:D04110. <https://doi.org/10.1029/2007JD009132>
- Chou MD, Lee KT (1996) Parameterizations for the absorption of solar radiation by water vapor and ozone. *J Atmos Sci* 53:1203–1208
- Chou MD, Lee KT, Tsay SC, Fu Q (1999) Parameterization for cloud longwave scattering for use in atmospheric models. *J Clim* 12(1):159–169
- Condom T, Rau P, Espinoza JC (2011) Correction of TRMM 3B43 monthly precipitation data over the mountainous areas of Peru during the period 1998–2007. *Hydrol Process* 25:1924–1933
- Corrales-Suastegui A, Fuentes-Franco R, Pavia EG (2020) The mid-summer drought over Mexico and Central America in the 21st century. *Int J Climatol*. <https://doi.org/10.1022/joc.6296>
- Danielson JJ, Gesch DB (2011) Global multi-resolution terrain elevation data. Report number: Open-File Report 2011–1073. <https://doi.org/10.3133/ofr20111073>
- Davis RE, Hayden BP, Gay DA, Phillips WL, Jones GV (1996) The North Atlantic subtropical anticyclone. *J Clim* 10:728–744
- D’Croz L, O’Dea A (2007) Variability in upwelling along the Pacific shelf of Panama and implications for the distribution of nutrients and chlorophyll. *Estuar Coast Shelf Sci* 73:325–340
- Durán-Quesada AM, Gimeno L, Amador J (2017) Role of moisture transport for Central American precipitation. *Earth Syst Dynam* 8:147–161
- Ek MB, Mitchell KE, Lin Y, Rogers E, Grunmann P, Koren V, Gayno G, Tarpley JD (2003) Implementation of Noah land surface model advances in the national centers for environmental prediction operational mesoscale Eta model. *J Geophys Res Atmos*. <https://doi.org/10.1029/2002JD003296>
- Enfield DB, Alfaro EJ (1999) The dependence of Caribbean rainfall on the interaction of the tropical Atlantic and Pacific Oceans. *J Clim* 12:2093–2103. [https://doi.org/10.1175/1520-0442\(1999\)012%3c2093:TDOCRO%3e2.0.CO;2](https://doi.org/10.1175/1520-0442(1999)012%3c2093:TDOCRO%3e2.0.CO;2)
- Ezer T, Arango H, Shchepetkin AF (2002) Developments in terrain-following ocean models: intercomparisons of numerical aspects. *Ocean Model* 4:249–267
- Fiedler PC (2002) The annual cycle and biological effects of the Costa Rica Dome. *Deep-Sea Res I* 49:321–338
- Fratantoni DF (2001) North Atlantic surface circulation during the 1990’s observed with satellite-tracked drifters. *J Geophys Res* 106:22067–22093
- Fuentes-Franco R, Coppola E, Giorgi F, Pavia EG, Diro GT, Graef F (2015) Inter-annual variability of precipitation over southern Mexico and Central America and its relationship to sea surface temperature from a set of future projections from CMIP5 GCMs and RegCM4 CORDEX simulations. *Clim Dyn* 45:425–440. <https://doi.org/10.1007/s00382-014-2258-6>
- Gimeno L, Stohl A, Trigo RM, Dominguez F, Yoshimura K, Yu L et al (2012) Oceanic and terrestrial sources of continental precipitation. *Rev Geophys* 50(4):4003
- Giorgi F (2019) Thirty years of regional climate modeling: where are we and where are we going next? *J Geophys Res*. <https://doi.org/10.1029/2018JD030094>
- Glazer R, Misra V (2018) Ice versus liquid water saturation in simulations of the Indian summer monsoon. *Clim Dyn*. <https://doi.org/10.1007/s00382-018-4116-4>
- Haidvogel DB, Arango HG, Hedstrom K, Beckmann A, Malanotte-Rizzoli P, Shchepetkin AF (2000) Model evaluation experiments in the North Atlantic Basin: simulations in nonlinear terrain-following coordinates. *Dyn Atmos Oceans* 32(3):239–281
- Ham S, Yoshimura K, Li H (2016) Historical dynamical downscaling for East Asia with the atmosphere and ocean coupled regional model. *J Meteor Soc Japan* 94A:199–208. <https://doi.org/10.2151/jmsj.2015-046>
- Heather HM, Bourassa MA (2014) The effects of gap-wind-induced vorticity, the monsoon trough, and the ITCZ on East Pacific tropical cyclogenesis. *Mon Wea Rev* 142:1312–1325
- Hidalgo HG, Durán-Quesada AM, Amador JA, Alfaro EJ (2015) The Caribbean low-level jet, the inter-tropical convergence zone and precipitation patterns in the intra-Americas sea: a proposed dynamical mechanism. *Geogr Ann Ser B* 97(1):41–59
- Hirpa FA, Gebremichael M, Hopson T (2010) Evaluation of high-resolution satellite precipitation products over very complex terrain in Ethiopia. *J Appl Meteor Climatol* 49:1044–1051
- Hong SY, Pan HL (1996) Nonlocal boundary layer vertical diffusion in a medium-range forecast model. *Mon Weather Rev* 124(10):2322–2339
- Juang HM, Kanamitsu M (1994) The NMC nested regional spectral model. *Mon Weather Rev* 122:3–26
- Kain J, Fritsch M (1993) Convective parameterization for mesoscale models: the Kain-Fritsch scheme. *Meteorol Monogr* 24:165–170
- Kanamaru H, Kanamitsu M (2007) Scale-selective bias correction in a downscaling of global reanalysis using a regional model. *Mon Weather Rev* 135:334–350
- Kanamitsu M, Ebisuzaki W, Woollen J, Yang SK, Hnilo JJ, Fiorino M, Potter GL (2002) NCEP–DOE AMIP-II reanalysis (R-2). *Bull Am Meteor Soc* 83:1631–1643. <https://doi.org/10.1175/BAMS-83-11-1631>
- Kanamitsu M, Yoshimura K, Yhang BY, Hong SY (2010) Errors of interannual variability and trend in dynamical downscaling of reanalysis. *J Geophys Res Atmos*. <https://doi.org/10.1029/2009JD013511>
- Kessler WS (2006) The circulation of the eastern tropical Pacific: a review. *Prog Oceanogr* 69:181–217
- King FD (1986) The dependence of primary production in the mixed layer of the eastern tropical Pacific on the vertical transport of nitrate. *Deep-Sea Res I* 33:733–754
- Landsea CW, Franklin JL (2013) Atlantic hurricane database uncertainty and presentation of a new database format. *Mon Wea Rev* 141:3576–3592
- Large WG, McWilliams JC, Doney SC (1994) Oceanic vertical mixing: a review and a model with a nonlocal boundary layer parameterization. *Rev Geophys* 32(4):363–403
- Legeckis R (1988) Upwelling off the gulfs of Panama and Papagayo in the tropical Pacific during March 1985. *J Geophys Res* 93:15485–15489
- Li H, Misra V (2014) Thirty-two-year ocean–atmosphere coupled downscaling of global reanalysis over the Intra-Americas Seas. *Clim Dyn*. 43:2471–2489. <https://doi.org/10.1007/s00382-014-2069-9>
- Li H, Kanamitsu M, Hong S-Y, Yoshimura K, Cayan DR, Misra V (2014) A high-resolution ocean-atmosphere coupled downscaling of the present climate over California. *Clim Dyn* 42(3–4):701–714. <https://doi.org/10.1007/s00382-013-1670-7>
- Magaña V, Amador JA, Medina S (1999) The midsummer drought over Mexico and Central America. *J Clim* 12(6):1577–1588
- Maldonado T, Alfaro EJ, Hidalgo HG (2018) A review of the main drivers and variability of Central America’s climate and seasonal forecast systems. *Rev Biol Trop* 66:S153–175
- Mapes BE, Liu P, Buening N (2005) Indian monsoon onset and the Americas midsummer drought: out-of-equilibrium responses to smooth seasonal forcing. *J Climate* 18:1109–1115
- McCreary JP, Lee HS, Enfield DB (1989) The response of the coastal ocean to strong offshore winds: with application to circulations in the Gulfs of Tehuantepec and Papagayo. *J Mar Res* 47:81–109
- Mellor GL, Yamada T (1982) Development of a turbulence closure model for geophysical fluid problems. *Rev Geophys* 20:851–875. <https://doi.org/10.1029/RG020i004p00851>

- Misra V (2020) Regionalizing global climate variations: a study of the Southeastern US regional climate. Elsevier, p 324 (ISBN: 978-0-12-821826-6)
- Misra V, Li H, Kozar M (2014) The precursors in the intra-Americas Seas to seasonal climate variations over North America. *J Geophys Res (oceans)* 119(5):2938–2948. <https://doi.org/10.1002/2014JC009911>
- Misra V, Groenen D, Bhardwaj A, Mishra A (2016) The warm pool variability of the tropical northeast Pacific. *Int Climatol*. <https://doi.org/10.1002/joc.4658>
- Misra V, Mishra A, Bhardwaj A (2017) High-resolution regional-coupled ocean-atmosphere simulation of the Indian summer monsoon. *Int J Climatol*. <https://doi.org/10.1002/joc5034>
- Misra V, Mishra A, Bhardwaj A (2018) Simulation of the intraseasonal variations of the Indian summer monsoon in a regional coupled ocean-atmosphere model. *J Clim* 31:3167–3185
- Moorthi S, Suarez MJ (1992) Relaxed Arakawa-Schubert. A parameterization of moist convection for general circulation models. *Mon Weather Rev* 120(6):978–1002
- Morris SS, Gonzales ON, Carletto C, Munguia M, Medina JM, Wodon Q (2002) Hurricane Mitch and the livelihoods of the rural poor in Honduras. *World Dev* 30:49–60
- Munoz E, Busalacchi AJ, Nigam S, Ruiz-Barradas A (2008) Winter and summer structure of the Caribbean low-level jet. *J Climate*. <https://doi.org/10.1175/2007JCLI1855.1>
- NOAA National Geophysical Data Center (2006) 2-minute gridded global relief data (ETOPO2)v2. NOAA Natl Cent Environ Inf. <https://doi.org/10.7289/V5J1012Q>
- Perez JS, Cervantes HH, Gutierrez G (2000) Gyres observed with altimetry in the tropical Pacific Ocean. SPIE proceedings, vol. 4172, Remote Sensing of the Ocean and the Sea Ice, <https://doi.org/10.1117/12.411707>
- Poveda G, Mesa OJ (1999) The westerly Colombian low-level jet (“CHOCO”) and two other low-level jets over Colombia: Climatology and variability during ENSO phases (In Spanish), *Revista Academia Colombiana de Ciencias, Exactas, Físicas y Naturales*, 23(89): 517–528
- Quirós-Badilla E, Hidalgo-León HG (2016) Variabilidad y conexiones climáticas de la zona de convergencia intertropical del Pacífico este. *Temas Meteorológicos y Oceanográficos*, 15(1): 21–36
- Retana JA (2012) Eventos hidrometeorológicos extremos lluviosos en Costa Rica desde la perspectiva de la adaptación al cambio en el clima. *Ambientales* 44: 5–16.
- Reynolds RW, Smith TM, Liu C, Chelton DB, Casey KS, Schlax MG (2007) Daily high-resolution-blended analyses for sea surface temperature. *J Clim* 20:5473–5496. <https://doi.org/10.1175/JCLI-D-14-00293.1>
- Romero-Centeno R, Zavala-Hidalgo J, Gallegos A, O'Brien JJ (2003) Isthmus of Tehuantepec wind climatology and ENSO signal. *J Clim* 16:2628–2639
- Saha S et al (2010) The NCEP climate forecast system reanalysis. *Bull Am Soc* 91:1015–1058. <https://doi.org/10.1175/2010BAMS3001.1>
- Schultz DM, Bracken WE, Bosart LF (1998) Planetary- and synoptic-scale signatures associated with Central American cold surges. *Mon Weather Rev* 126(1):5–27
- Selman C, Misra V (2015) Simulating diurnal variations over the southeastern United States. *J Geophys Res Atmos* 120:180–198. <https://doi.org/10.1002/2014JD021812>
- Shchepetkin AF, McWilliams JC (2005) The regional oceanic modeling system (ROMS): a split-explicit, free-surface, topography-following-coordinate oceanic model. *Ocean Model* 9(4):347–404
- Sheng J, Tang L (2003) A numerical study of circulation in the Western Caribbean Sea. *J Phys Oceanogr* 33:2049–2069
- Shige S, Nakano Y, Yamamoto MK (2017) Role of orography, diurnal cycle, and intraseasonal oscillation in summer monsoon rainfall over the Western Ghats and Myanmar Coast. *J Climate* 30:9365–9381. <https://doi.org/10.1175/JCLI-D-16-0858.1>
- Spencer N, Urquhart M-A (2018) Hurricane strikes and migration: evidence from storms in Central America and the Caribbean. *Weather Clim Soc* 10:569–577
- Sun Q, Miao C, Duan Q, Ashouri H, Sorooshian S, Hsu KL (2018) A review of global precipitation data sets: data sources, estimation, and intercomparisons. *Rev Geophys* 56(1):79–107. <https://doi.org/10.1002/2017RG000574>
- Tatsumi Y (1986) A spectral limited area model with time dependent lateral boundary conditions and its application to a multi-level primitive equation model. *J Meteor Soc Jpn* 64:637–663
- Tiedtke M (1983) The sensitivity of the time-mean large-scale flow to cumulus convection in the ECMWF model. Proceedings of ECMWF workshop on convective in large-scale models. European Centre for Medium-Range Weather Forecasts, Reading, United Kingdom, pp 297–316
- Timmermann A et al (2007) The influence of a weakening of the Atlantic meridional overturning circulation on ENSO. *J Climate* 20:4899–4919
- Torres-Alavez JA, Das S, Corrales-Suategui A, Coppola E, Giorgi F, Raffaele F, Bukovsky MS, Ashfaq M, Salinas JA, Sines T (2021) Future projections in the climatology of global low-level jets from CORDEX-CORE simulations. *Clim Dyn* 57:1551–1569
- Ullrich PA, Zarzycki CM (2017) TempestExtremes v1.0: a framework for scale-insensitive pointwise feature tracking on unstructured grids. *Geosci Model Dev Discuss*. <https://doi.org/10.5194/gmd-2016-217>
- Umlauf L, Burchard H (2003) A generic length-scale equation for geophysical turbulence models. *J Mar Res* 61(2):235–265
- Wang C (2007) Variability of the Caribbean low-level jet and its relations to climate. *Clim Dyn* 29:411–422
- Wang C, Enfield DB (2001) The tropical western hemisphere warm pool. *Geophys Res Lett* 28:1635–1638
- Wang C, Lee S-K, Enfield DB (2007) Impact of the Atlantic warm pool on the summer climate of the Western Hemisphere. *J Clim* 20(20):5021–5040
- Wang C, Lee S-K, Enfield DB (2008) Climate response to anomalously large and small Atlantic warm pools during the summer. *J Climate* 21:2437–2450
- Webster S, Brown AR, Cameron DR, Jones CP (2003) Improvements to the representation of orography in the Met Office Unified Model. *Quart Roy Soc* 129:1989–2010
- Wyrтки K (1964) Upwelling in the Costa Rica Dome. *Fish Bull* 63:355–372
- Xie P, Yatagai A, Chen M, Hayasaka T, Fukushima Y, Liu C, Yang S (2007) A gauge based analysis of daily precipitation over East Asia. *J Hydrometeorol* 8:607–626. <https://doi.org/10.1175/JHM583.1>
- Xie S-P, Okumura Y, Miyama T, Timmermann A (2008) Influences of Atlantic climate change on the tropical Pacific via the Central America Isthmus. *J Climate* 21:3914–3928
- Yorgun MS, Rood RB (2014) An object-based approach for quantification of GCM biases of the simulation of orographic precipitation. Part I: idealized simulations. *J Clim* 27:9139–9154. <https://doi.org/10.1175/JCLI-D-14-00051.1>
- Zhao Q, Carr FH (1997) A prognostic cloud scheme for operational NWP models. *Mon Weather Rev* 125(8):1931–1953